



Particle tracking schemes for micron particle deposition in a 90° pipe bend and nasal airway geometry

Patrick Warfield-McAlpine ^a, David F. Fletcher ^b, Kiao Inthavong ^{a,*}

^a Mechanical & Automotive Engineering, School of Engineering, RMIT University, PO Box 71, Bundoora, 3083, Australia

^b School of Chemical and Biomolecular Engineering, The University of Sydney, NSW 2006, Australia

ARTICLE INFO

Editor: Dr. Chris Hogan

Keywords:

Nasal cavity

CFD

Turbulence dispersion

Particle deposition

ABSTRACT

Computational studies of micron particle deposition is used to predict inhaled particles through the nasal cavity for understanding drug delivery or toxicology risks. To ensure reliable results in future studies, this study evaluated particle tracking schemes and determined the most appropriate settings for predicting micron particle deposition in a pipe bend and nasal cavity geometry. Micron particles were injected into a fully developed 90° pipe bend under a turbulent flow regime with Reynolds number, $Re = 10,000$, for comparison with existing data in the literature. Similarly, the micron particles were released into a more complex geometry, a human nasal cavity.

The study found that although the high-resolution tracking is the default and preferred option set out by Ansys-Fluent, the 5 μm particle tested travelled further than when the high-resolution tracking was off. This was rectified by setting the wall nodal velocity to zero. All particle tracking schemes performed well and were suitable for predicting deposition for particle diameters $> 5\mu\text{m}$, with high-resolution tracking and setting the wall nodal velocity to zero. However, the results become sensitive to the particle scheme when dealing with particle diameters $< 5\mu\text{m}$. The lower-order schemes overpredict deposition, while the higher-order schemes have zero deposition in the pipe bend unless the wall nodal velocity is set to zero. This study provides a list of recommended settings to best simulate particle deposition efficiency in Ansys Fluent (version 2023R2), although future releases of the CFD software may incorporate these settings as default options.

1. Introduction

Particle deposition in internal flows is prevalent in many industrial settings, such as fouling or erosion of pipes in heat exchangers and turbine blades. Furthermore, airborne particles travel through ventilation systems and of recent interest is the viral aerosol dispersion in indoor environments. While particle deposition is ubiquitous for industrial applications, its application to biomedical fields is also commonplace. This includes nasal and pulmonary drug delivery through the internal respiratory airway or the negative impacts of inhalation exposure to hazardous airborne particulates (Abouali et al., 2012; Inthavong et al., 2021; Si, Xi, Kim, Zhou, & Zhong, 2013; Yousefi, Inthavong, & Tu, 2015).

Recently, an unprecedented volume of research was published on computational modelling of viral aerosol dispersion and deposition in indoor environments and the respiratory airway (Else, 2020; Ioannidis, Salholz-Hillel, Boyack, & Baas, 2021) due to the COVID-19 pandemic. However, Dinis-Oliveira (2020) noted that the rush to publish may have jeopardised the previously

* Corresponding author.

E-mail address: kiao.inthavong@rmit.edu.au (K. Inthavong).

established peer-review standards, leading to retractions due to concerns about the reliability of the results (Abritis, Marcus, & Oransky, 2021; Teixeira da Silva, Bornemann-Cimenti, & Tsigaris, 2021). To ensure reliable results in future studies, this study aims to explore particle tracking schemes for aerosol dispersion and to determine the most appropriate case settings for micron particle dispersion and its deposition in a pipe bend and nasal cavity model.

Computational Fluid Dynamics (CFD) simulations (Dastan, Abouali, & Ahmadi, 2014; Schroeter, Garcia, & Kimbell, 2011) are commonly used to predict fluid flow and particle behaviour, in lieu of invasive, and challenging *in-vivo* experiments using human subjects. Before moving into a complex geometry, such as the human respiratory airway, simulations can be implemented on simple, well-known geometries initially to investigate the fundamental mechanisms of particle deposition and to validate the accuracy of computational models. This includes deposition studies in pipe and channel flows configurations (Ahmadi, Ounis, & McLaughlin, 1992; Berrouk & Laurence, 2008; Breuer, Baytekin, & Matida, 2006; Dehbi, 2008a, 2008b; Inthavong, Tian, & Tu, 2016; Jafari, Salmanzadeh, Rahnama, & Ahmadi, 2010; Matida, Nishino, & Torii, 2000; Mehel, Tanière, Oesterlé, & Fontaine, 2010; Wang & Squires, 1996; Zhang, Ahmadi, Fan, & McLaughlin, 2001). These studies have contributed to the development and improvement of computational models used in CFD simulations of particle dispersion and have provided the validation for particle deposition predictions in more complex geometries like the nasal airway.

Early studies of aerosol deposition in the upper respiratory system used idealised geometries and flow conditions and characterised the particle deposition within the respiratory system (Hofmann, 2011; Longest & Holbrook, 2012; Longest & Vinchurkar, 2007b; Nowak, Kakade, & Annapragada, 2003; Zhang, Kleinstreuer, Donohue, & Kim, 2005). Such models represented the upper respiratory anatomy as a piping network. Later, with advances in Computed Tomography (CT) scans, realistic models emerged that provide a more accurate representation of the respiratory airway (Corley et al., 2012; Dong et al., 2019; Ghalati et al., 2012; Koullapis, Kassinos, Bivolarova, & Melikov, 2016; Lambert, O'shaughnessy, Tawhai, Hoffman, & Lin, 2011; Shang, Inthavong, & Tu, 2015).

Studies of particle deposition in the nasal cavity have identified inertial impaction as the primary deposition mechanism for micron particles (Calmet et al., 2018; Inthavong, Ge, Se, Yang, & Tu, 2011; Kimbell et al., 2007; Schroeter, Kimbell, & Asgharian, 2006; Shang & Inthavong, 2019), while particles in the submicron range, will deposit by Brownian diffusion (Garcia, Schroeter, & Kimbell, 2015; Ghalati et al., 2012; Gonda & Gipps, 1990; Inthavong, Ge, et al., 2011; Shi, Kleinstreuer, & Zhang, 2008). Inertially driven micron particles will impact walls when there is sufficient change in the flow direction of streamlines, and the classical pipe bend study demonstrates this phenomenon (Ball & Mitchell, 1992; Pui, Romay-Novas, & Liu, 1987). Inertial particle deposition is proportional to the particle's aerodynamic diameter to the square power, and the mean air stream velocity, neatly encapsulated by the particle Stokes number ($St = \frac{\rho_p d_p^2 U}{18\mu_g D}$). Smaller particles (e.g., 1 to 5 μm) lack sufficient inertia while exhibiting a shorter particle relaxation time, allowing the particle trajectories to adjust to changes in flow streamlines more readily. This means they are sensitive to turbulent fluctuations in the flow field. Many studies of steady-state flows using Reynolds Averaged Navier-Stokes (RANS) based turbulence models have demonstrated the requirement of damping the turbulence kinetic energy (TKE) in the near wall region (Inthavong, Tu, & Heschl, 2011; Liu, Matida, Gu, & Johnson, 2007; Matida, Finlay, Lange, & Grgic, 2004; Wang & James, 1999), to obtain accurate solutions, based on the profile obtained through direct numerical simulation (DNS) data of channel flows (Kim, Moin, & Moser, 1987; Moser, Kim, & Mansour, 1999).

Computational mesh structures and type were shown to have a significant effect on the flow field solution accuracy and particle deposition (Longest & Vinchurkar, 2007a; Vinchurkar & Longest, 2008). Subsequent studies (Bass & Longest, 2018; Frank-Ito, Wofford, Schroeter, & Kimbell, 2016; Inthavong, Chetty, Shang, & Tu, 2018) were performed to provide recommendations on mesh design for airway geometry flows that is helpful in understanding the effects of meshing on airflow and particle transport in the airways. In theory, if the geometry is modelled with sufficient mesh elements, such that the flow field is resolved correctly, further mesh refinements should not influence the flow field nor the particle deposition, thus achieving mesh independence.

While past studies have provided recommendations for meshing types and modifications of the turbulence in the near wall region to improve particle deposition in human airway geometries, this study investigated the influence of four particle trajectory integration schemes within the Ansys-Fluent software package. This study aims to provide recommended settings and best practices to predict micron particle deposition in simple and complex internal flow geometries. This will be achieved by assessing the particle integration schemes, and correcting any nonphysical flow representation from modelling assumptions. Micron particles were simulated using particles with diameters in the range of 1–26 μm at unit density. A 90° pipe bend and a human nasal cavity were investigated based on those described in the available literature.

2. Methodology

2.1. Geometry models and meshing

A 90° pipe bend model was created (see Fig. 1) in Ansys SpaceClaim (v23R1). The pipe has a bend curvature ratio of 5.6 for comparison with geometries used in experimental and numerical literature (Berrouk & Laurence, 2008; Breuer et al., 2006; Pui et al., 1987). Following the studies from Berrouk and Laurence (2008) and Breuer et al. (2006) a pipe diameter (D) of 0.02 m was selected with entry and exit lengths of $1D$ and $2D$ to minimise artificial flow induced by the bend, Fig. 1a. The surfaces were separated into the straight inlet, pipe bend, and exit regions to differentiate local particle deposition.

A nasal airway model was generated from a computed tomography (CT) scan of a healthy 25-year-old, Asian female (161 cm height, 53 kg mass, without nasal septum deviation, turbinate hypertrophy or sinusitis) at resting conditions. The CT data were acquired using a Siemens Dual Source CT scanner with image parameters of $0.39 \times 0.39 \text{ mm}$ pixel size, 512×512 pixels image

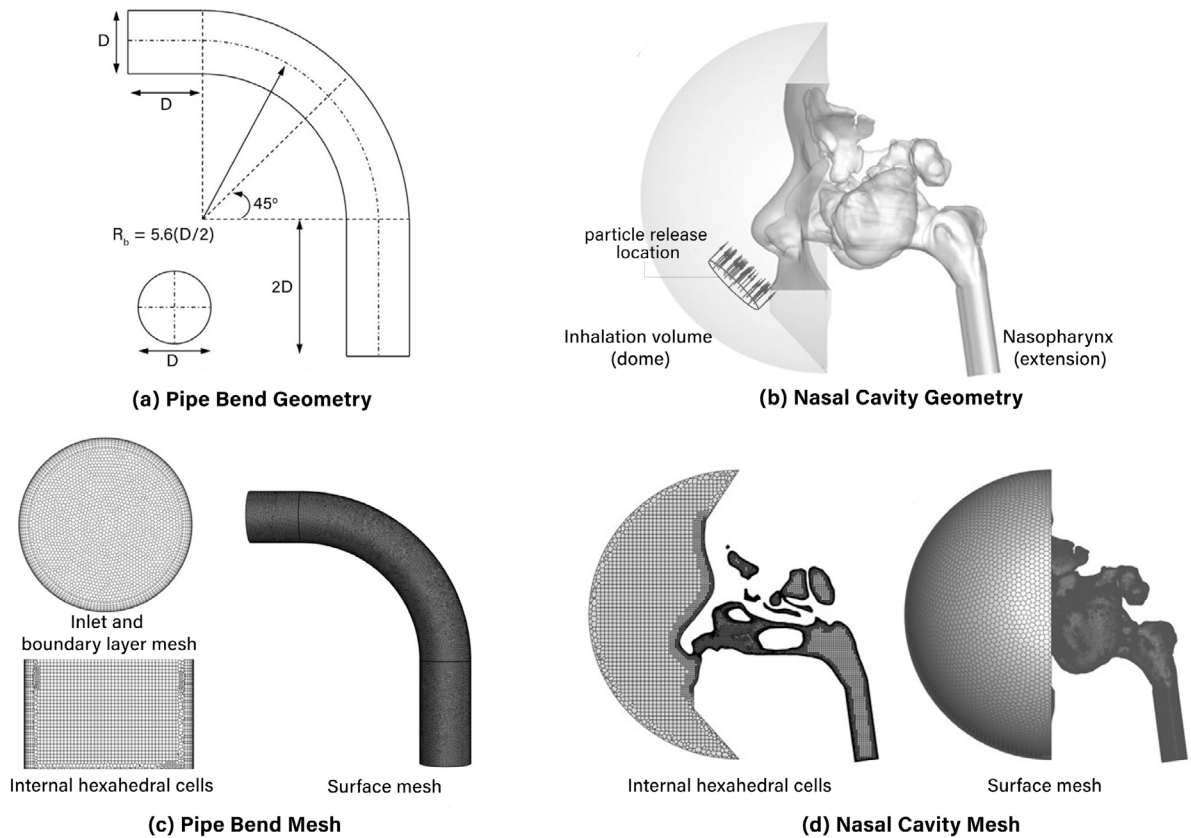


Fig. 1. Geometry and mesh. (a): Normalised pipe bend geometry (b): Nasal cavity geometry including inhalation volume and Nasopharynx extension, (c): Pipe bend mesh: Internal hexahedral cells and polyhedral surface layer, (d): Nasal cavity mesh: internal hexahedral structure and surface polyhedrals.

dimensions and 0.5 mm slice thickness, where the model has been used in previous studies (Bradshaw et al., 2022; Inthavong, Shang, Wong, & Singh, 2020; Senanayake et al., 2021, 2023; Shrestha, Salati, Fletcher, Singh, & Inthavong, 2021; Zhang et al., 2019). The CT scans were processed using the 3D Slicer segmentation software. Although minimal flow has been observed entering the paranasal sinuses, they were included for completeness. A registered ENT performed the segmentation process manually (from earlier studies) and involved segmenting individual anatomical regions (outer nose and face, main passage, sinuses, and nasopharynx). The model was cleaned by locally smoothing, removing spikes, and filling in small gaps. The model was exported to Geomagic, and a wrapping function was employed to produce NURBS surface patches and remove gaps that occur from reading the CAD file.

Although minimal flow has been observed entering the paranasal sinuses, they were included for completeness. A frontal dome representing a volume of air and an artificial extension at the nasopharynx was created to ensure proper boundary behaviour, Fig. 1b. The frontal dome with the volume of air has been reported to be necessary (Li, Inthavong, Ge, & Tu, 2013; Shang et al., 2015) to allow a natural inhalation condition at the nostril inlets, which are non-planar, rather than providing a uniform cross-section plane inlet condition when the dome volume of air is omitted. A mesh wrapping task was performed using the Fault-tolerant workflow in the Ansys-Fluent meshing software to ensure the model was watertight.

All geometry models were meshed with hybrid poly-hexcore cells with prism layers at the wall where the first cell height was set to correspond to a $y^+ \approx 1$, satisfying the boundary layer requirements of the $k\omega$ -SST model (Menter, 1993). One peel layer connects the polyhedral or prism cells to the hexahedral cells. The choice of a poly-hexcore mesh was to take advantage of hexahedral cells in the bulk flow region for their higher accuracy due to the perfectly orthogonal structure leading to reduced numerical diffusion and computing power compared with tetrahedral cells (Longest & Vinchurkar, 2007a; Vinchurkar & Longest, 2008). As hexahedral cells are difficult to apply on curved and complex boundaries, polyhedrals were placed on the curved boundary walls of the nasal cavity. Polyhedrals also calculate gradients more accurately as the shapes have much less control-volume shape dependency. For the same grid resolution, there is a total face count reduction. This total face count reduction helps result in faster computing times.

Fig. 1b shows the surface mesh with polyhedrals, while the cross-section image shows the hexcore elements with prism layers at the walls. Details of the meshing are summarised in Tables 1 and 2.

The mesh was created to produce a first cell node of $y^+ \approx 1$ in the region with the greatest wall shear stress with the aim of ensuring 3–4 prism cells inside the viscous sublayer. The first layer height was held constant throughout the domain. For the pipe, the wall y^+ value was predominantly in the range of 0.5 to 0.9; for the nasal cavity, the range was 0.6 to 1.8 (see Fig. 2). While

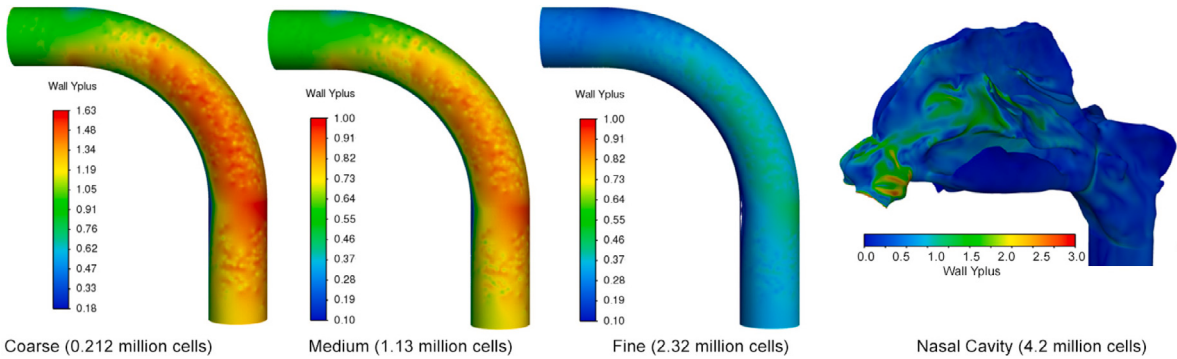


Fig. 2. Wall surface y^+ contours for the coarse, medium, and fine meshed models for the 90° pipe bend, and the nasal cavity model. The models exhibited y^+ contours of less than 5 suggesting the first mesh node is within the viscous sublayer.

Table 1
Mesh settings for the pipe bend and nasal airway geometry model.

Geometry	Prism layers	First height (mm)	First cell aspect ratio	Cells (Mil.)	Meshing
Pipe 90° bend	8	0.021	14.6	0.212	coarse
	8	0.021	14.6	1.13	medium
	8	0.021	14.6	2.32	fine
Nasal cavity	8	0.06	0.6 to 1.8	4.2	–

Table 2
Mesh settings for the pipe geometry models used for different prism layers.

Geometry	Prism layers	First height (mm)	First cell aspect ratio	Cells (Mil.)	y^+
Pipe 90° bend	5	0.034	8.67	0.84	0.6 to 1.4
	8	0.021	14.6	1.13	0.5 to 0.9
	12	0.011	23.3	1.33	0.3 to 0.5

Table 3
Flow conditions for the geometry models.

Geometry	Flow rate	Viscous model
Pipe 90° bend	$Re = 1,000$	Laminar
	$Re = 10,000$	$k\omega$ -SST
Nasal cavity	30 L/min	$k\omega$ -SST
	60 L/min	$k\omega$ -SST

this is applicable as the ω -equation can be integrated through the viscous sublayer, the Fluent solver now applies a y^+ insensitive wall treatment by blending the viscous sublayer formulation and the logarithmic layer formulation based on y^+ .

2.2. Fluid flow modelling

A range of flow conditions were applied to the geometry models that included laminar and turbulent flows at different Reynolds numbers to compare against reported data in the literature. **Table 3** summarises the different flow conditions.

Fully developed flow profiles were applied for the pipe flows. The fully developed laminar flow was created using the analytical solution:

$$u(r) = 2u_{ave} \left(1 - \frac{r^2}{R^2} \right) \quad (1)$$

where r is the radial distance from the pipe centre, R is the pipe radius, and u_{ave} is the mean velocity.

The fully developed turbulent flow was produced by performing a precursor periodic flow in a smaller straight pipe sub-section. The velocity components, TKE and specific dissipation rate (ω) for the turbulent flow were exported and applied as the inlet boundary conditions of the pipe bend geometry. A steady nasal inhalation was simulated by applying a zero total pressure at the frontal dome and a mass-flow rate to the outlet of the nasopharynx extension, **Fig. 1**.

The fluid flow was modelled in steady-state using the conservation of mass and momentum for incompressible flow as outlined below:

$$\frac{\partial}{\partial x_i} (\rho u_i) = 0 \quad (2)$$

$$u_j \frac{\partial u_i}{\partial x_j} = -\frac{1}{\rho} \frac{\partial p}{\partial x_i} + \frac{\partial}{\partial x_j} \left((\nu + \nu_T) \frac{\partial u_i}{\partial x_j} \right) \quad (3)$$

where u_i is the i th component of the time-averaged velocity vector, p is the pressure, ρ is the air density and ν and ν_T are the air kinematic and turbulent viscosities, respectively.

Turbulence was modelled using the $k\omega$ -SST model (Menter, 1993). This model applies a blending function to combine the standard $k\text{-}\epsilon$ and $k\text{-}\omega$ models. The model approximates the flow field by using the kinematic eddy viscosity calculated from the TKE and specific dissipation rate. Furthermore, it provides a y^+ -insensitive wall treatment, thus, no wall functions are needed.

The pressure–velocity solution was obtained using the Coupled solver. Spatial discretisation of gradients used the least squares cell-based method, the second-order method for pressure and second-order upwind methods for momentum, TKE and specific dissipation rate, which are the default Ansys-Fluent settings. The solution was run in steady-state mode until the locally-scaled residuals of all variables fell below 1×10^{-6} .

2.3. Discrete phase modelling

Particle trajectory equations

Discrete phase modelling was performed using the one-way coupled Lagrangian model. This model simulates the continuous phase first and then tracks the trajectories of individual particles by integrating the force balance on each particle:

$$m_p \frac{d\mathbf{u}_p^p}{dt} = \mathbf{f}_D \quad (4)$$

where superscript p refers to the particle phase, and \mathbf{f}_D refers to the drag force per unit mass represented by the Stokes drag law:

$$\mathbf{f}_D = m_p \frac{(\mathbf{u}_i^g - \mathbf{u}_i^p)}{\tau_p} \quad (5)$$

where superscripts g and p refer to the fluid and particle phases, respectively, and τ_p is the particle response time given by:

$$\tau_p = \frac{a_p^2 \rho_p C_c}{18\mu} \frac{24}{C_d \text{Re}} \quad (6)$$

where C_d is the drag coefficient and C_c is the Cunningham correction factor which is used to adjust the Stokes drag law to represent submicron particles but is not required in this study.

2.3.1. Particle trajectory integration schemes

The particle trajectories in the discrete phase model are solved iteratively by a step-wise integration over discrete time steps. The particle velocity is solved by integrating wrt time at each point along the trajectory. The particle trajectory is approximated by Eq. (7) below (note only a single component is shown for simplicity):

$$\frac{dx}{dt} = u_p \quad (7)$$

The particle momentum balance Eq. (4) can be re-written in terms of the drag force per unit mass:

$$\frac{du_p}{dt} = \frac{1}{\tau_p} (u - u_p) \quad (8)$$

The Ansys-Fluent solver computes the trajectory by four integration schemes: Analytic, Implicit, Trapezoidal and Runge–Kutta. Eq. (7) and Eq. (8) form a set of coupled ordinary equations. Under the assumption of constant u , and τ_p an analytical integration can be performed to solve Eq. (7) and Eq. (8) leading to Eq. (9) and Eq. (10) for the new particle velocity (u_p^{n+1}) and location (x_p^{n+1}), respectively. This study removed additional body forces that may be applied to the particle by external fields, i.e., gravity, but drag was included.

$$u_p^{n+1} = u^n + \exp \left(-\frac{\Delta t}{\tau_p} \right) (u_p^n - u^n) \quad (9)$$

$$x_p^{n+1} = x_p^n + \Delta t u^n + \tau_p \left(1 - e^{-\frac{\Delta t}{\tau_p}} \right) (u_p^n - u^n) \quad (10)$$

where u_p^n and u^n represent the particle and fluid velocity at the initial location.

Numerical integration can also be used to solve Eq. (7) and Eq. (8) using different particle trajectory discretisation schemes.

Applying the Euler Implicit discretisation scheme gives the following:

$$u_p^{n+1} = \frac{u_p^n + \Delta t \frac{u^n}{\tau_p}}{1 + \frac{\Delta t}{\tau_p}} \quad (11)$$

The Trapezoidal discretisation averages the velocity terms u_p and u , represented as the following equation:

$$\frac{u_p^{n+1} - u_p^n}{\Delta t} = \frac{1}{\tau_p (u^* - u_p^*)} \quad (12)$$

where the averages u_p^* , u^* and u^{n+1} are calculated from:

$$u_p^* = \frac{1}{2} (u_p^n + u_p^{n+1}) \quad (13)$$

$$u^* = \frac{1}{2} (u^n + u^{n+1}) \quad (14)$$

$$u^{n+1} = u^n + \Delta t u_p^n \cdot \nabla u^n \quad (15)$$

The particle velocity at the new location ($n + 1$), is then calculated by:

$$u_p^{n+1} = \frac{u_p^n \left(1 - \frac{1}{2} \frac{\Delta t}{\tau_p} \right) + \frac{\Delta t}{\tau_p} \left(u^n + \frac{1}{2} \Delta t u_p^n \cdot \nabla u^n \right)}{1 + \frac{1}{2} \frac{\Delta t}{\tau_p}} \quad (16)$$

The new particle location for the Implicit and Trapezoidal schemes is computed by Trapezoidal discretisation of Eq. (7):

$$x_p^{n+1} = x_p^n + \frac{1}{2} \Delta t (u_p^n + u_p^{n+1}) \quad (17)$$

The explicit Runge–Kutta scheme from [Cash and Karp \(1990\)](#) considers the ordinary differential equations as vectors, where the left hand side is the derivative \vec{y}' , and the right hand side is a function $\vec{f}(t, \vec{y})$.

$$\vec{y}' = \vec{f}(t, \vec{y}) \quad (18)$$

and

$$\vec{y}^{n+1} = \vec{y}^n + c_1 \vec{k}_1 + c_2 \vec{k}_2 + c_3 \vec{k}_3 + c_4 \vec{k}_4 + c_5 \vec{k}_5 + c_6 \vec{k}_6 \quad (19)$$

where:

$$\begin{aligned} \vec{k}_1 &= \Delta t \vec{f}(t, \vec{y}^n) \\ \vec{k}_2 &= \Delta t \vec{f}(t + a_2 \Delta t, \vec{y}^n + b_{21} \vec{k}_1) \\ \vec{k}_3 &= \Delta t \vec{f}(t + a_3 \Delta t, \vec{y}^n + b_{31} \vec{k}_1 + b_{32} \vec{k}_2) \\ \vec{k}_4 &= \Delta t \vec{f}(t + a_4 \Delta t, \vec{y}^n + b_{41} \vec{k}_1 + b_{42} \vec{k}_2 + b_{43} \vec{k}_3) \\ \vec{k}_5 &= \Delta t \vec{f}(t + a_5 \Delta t, \vec{y}^n + b_{51} \vec{k}_1 + b_{52} \vec{k}_2 + b_{53} \vec{k}_3 + b_{54} \vec{k}_4) \\ \vec{k}_6 &= \Delta t \vec{f}(t + a_6 \Delta t, \vec{y}^n + b_{61} \vec{k}_1 + b_{62} \vec{k}_2 + b_{63} \vec{k}_3 + b_{64} \vec{k}_4 + b_{65} \vec{k}_5) \end{aligned}$$

The coefficients a and b and are taken from [Cash and Karp \(1990\)](#).

The Analytic and Implicit (1st order) schemes are considered lower order and produce fast results as it is a one-step method that is stable at large time steps. However, they tend to be less accurate and depend on the time step size for accuracy. The Trapezoidal (2nd order) and Runge–Kutta (5th order) are higher-order schemes that perform multiple evaluations of their functions, thereby typically offering higher accuracy than lower-order schemes like the Euler Implicit method. However, as more evaluations between each time step are required, it makes them more computationally expensive. There is also a reliance on a sufficiently small time step as the results suffer from accuracy degradation when used with very large step sizes or in stiff ordinary differential equations, leading to potential numerical instability.

Ansys-Fluent provides an adaptive step-size control to adjust the step size based on the mesh and solution behaviour. It also provides an automatic particle trajectory integration setting that combines a lower-order and higher-order scheme with an accuracy control that modifies the length scale within a given error tolerance. However, as this study focused on the particle trajectory integration schemes, the adaptive step-size control and automatic switching schemes were not used.

The integration time step Δt was calculated using Ansys-Fluent's Step Length Factor equation,

$$\Delta t = \frac{\Delta t^*}{\lambda} \quad (20)$$

where λ is the step length factor, and Δt^* is a characteristic time that is related to an approximate time required for the particle to traverse the mesh cell. The default value of $\lambda = 5$ was used.

Discrete Random Walk (DRW) model

Particle turbulence dispersion is modelled by including the instantaneous fluid flow velocity. The fluid velocity term in Eq. (3) was derived by decomposing the instantaneous velocity into its mean and fluctuating components as:

$$\mathbf{u} = \bar{\mathbf{u}} + \mathbf{u}'(t) \quad (21)$$

where $\bar{\mathbf{u}}$ is the mean fluid velocity solved from the Navier–Stokes equations (Eqns 2, 3) and \mathbf{u}' is its fluctuating component determined by the DRW model.

In the Discrete Random Walk model, the fluctuating velocity components are discrete piecewise constant functions of time. To account for the randomness of turbulent flow, a Gaussian distributed function is applied, given by:

$$\mathbf{u}' = \zeta \sqrt{\mathbf{u}'^2} \quad (22)$$

where ζ is Gaussian random variable with variance of 1 and mean of 0. The random velocity fluctuation is then kept constant over an interval of time corresponding to the eddy lifetime. Thus, a particle is assumed to interact with discrete turbulent eddies within the flow field.

The term \mathbf{u}'^2 is the local root mean square (RMS) velocity fluctuation taken from the TKE term in the flow field and assuming isotropy:

$$\mathbf{u}' = v' = w' = \zeta \sqrt{\frac{2}{3} k} \quad (23)$$

Particle deposition onto walls in turbulent flows is dictated by what happens in the boundary layer. While turbulence can be approximated as being isotropic in the bulk near the wall, the turbulent velocity fluctuations are not isotropic, and the fluctuating normal velocity is much smaller than the streamwise or spanwise components; thus, inside the boundary layer, there is anisotropic behaviour.

The isotropic assumption in the $k\omega$ -SST model fails to replicate the physical behaviour of particle-turbulence interactions close to walls where anisotropic effects are significant (Dehbi, 2008b; Wang & James, 1999). Studies have shown this leads to an overprediction of the deposition of smaller inertial particles (Inthavong, Tu, & Heschl, 2011; Liu et al., 2007; Matida et al., 2000; Mofakham & Ahmadi, 2020), due to the higher value of the normal to the wall velocity fluctuation, v' as a result of the isotropic assumption. Based on fluid RMS velocities in the boundary layer computed from DNS data, Matida et al. (2004) provided a damping function to correctly match the v' profile as a function of the non-dimensional wall distance y^+ , given as:

$$k_{\text{damped}} = k [1 - \exp(-0.02y^+)]^2 \quad \text{for } y^+ < 30 \quad (24)$$

This correction applies the normal-to-the-wall function $f_v = 1 - \exp(-0.02y^+)$, from Wang and James (1999), to all three velocity components, which were originally developed for the channel flow but provides better values of fluctuations near the wall than those given when isotropy is assumed. This damping method implies isotropic damping across all three fluctuating velocity components (spanwise, streamwise, and normal directions) as the $k\omega$ -SST model is inherently isotropic. The method is applicable as we target the normal to the wall direction, which is the most influential velocity component exhibiting the greatest fluctuating magnitude among the three components. While the spanwise and streamwise components are also affected, their magnitudes are smaller, and their effect on deposition is negligible. The isotropic damping is a limitation of this method. An alternative is to apply the RSM (Reynolds Stress Model) turbulence model that allows individual velocity component damping. However, we have focused on the $k\omega$ -SST turbulence model as it is widely used among researchers.

2.4. Particle tracking numerical schemes

Particle injections and deposition

For the pipe bend, micron particle streams were injected using the face normal direction and randomised starting points on the inlet surface. Particle diameters ranged from 1–26 μm and were injected using 100,000 streams per particle size at an initial velocity magnitude of 7.3 m/s.

The analysis was repeated for the nasal cavity model by injecting stationary particles in front of the nasal cavity over a circular surface (see Fig. 1). Injected particle diameters ranged from 1–26 μm and were injected in streams of 100,000. The continuous phase flow field drew the particles into the nasal cavity using volumetric flow rates of 30 L/min and 60 L/min at the exit of the extended outlet zone.

Particle deposition in the pipe bend was calculated by the following equation based on the particle mass flow rate:

$$DE = \frac{\dot{m}_{p,\text{bend}}}{\dot{m}_{p,\text{bend}} + \dot{m}_{p,\text{after bend}}} \quad (25)$$

The pipe bend deposition was compared with the non-dimensional Stokes number (St) using the following equation:

$$St = \frac{\tau_p}{\tau_f} = \frac{\rho_p d_p^2}{18\mu_g} \frac{U}{D} \quad (26)$$

where U and D are characteristic velocity and length-scales of the flow, $\tau_p = \frac{\rho_p d_p^2}{18\mu_g}$ is the particle relaxation time, $\tau_f = \frac{U}{D}$ is the characteristic fluid timescale.

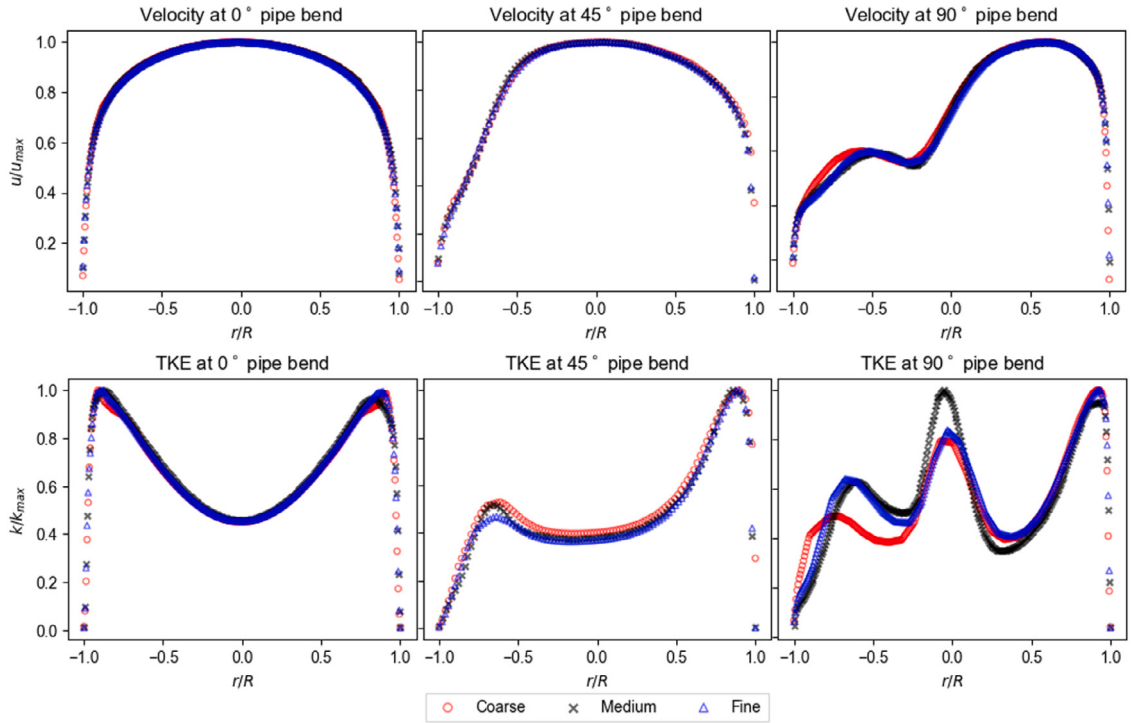


Fig. 3. Mesh independence for the pipe flow was carried out for a coarse, medium, and fine mesh having 0.212, 1.13, 2.32 million cells, respectively. Plots of (a) normalised velocity and (b) normalised turbulence kinetic energy are shown at the pipe bend at 0°, 45°, 90°.

The deposited mass was used to determine the deposition efficiency for the nasal cavity as follows

$$DE_{\text{nasal}} = \frac{\dot{m}_{\text{nasal cavity}}}{\dot{m}_{\text{nasal cavity}} + \dot{m}_{\text{after nasal cavity}}} \quad (27)$$

The nasal airway deposition efficiency was compared with the Inertial Parameter (units of $\mu\text{m}^2\text{cm}^3/\text{s}$) using the following equation:

$$\text{Inertial parameter} = d_a^2 Q \quad (28)$$

where d_a is the aerodynamic diameter (μm) and Q is volumetric flow rate (cm^3/s). The aerodynamic diameter of a particular particle is the diameter of a spherical particle with density of 1 g/cm^3 , that has the same settling velocity as the particle. Assuming a spherical shape this is defined as:

$$d_a = d_p \sqrt{\frac{\rho_p}{\rho_0}}$$

where ρ_p and ρ_0 are the particle and unit densities, respectively.

3. Results

3.1. 90° pipe bend

Mesh independence and pipe flow validation

Three meshed pipe models were created where each subsequent mesh exhibited a doubling in the minimum, and maximum sizes for the surface and doubling of the minimum and maximum cell lengths for the volume meshing using Fluent meshing. This produced three meshes consisting of 0.212 (coarse), 1.13 (medium), and 2.32 (fine) million cells. Velocity and turbulence kinetic energy profiles across the pipe bend for a steady flow rate of $Re = 10,000$ are shown in Fig. 3, from which it was concluded that the medium mesh of 1.13 million cells gave the best compromise of changes in predictions and cell count. In results presented later on the influence of the number of prism layers, the mesh resolution in the core region remained the same, and only the boundary layer mesh region was altered.

The fully developed turbulent flow profile at $Re = 10,000$ was obtained from a precursor simulation using a periodic flow to establish the fully developed state. The flow field was compared with data from Berrouk and Laurence (2008) where velocity line

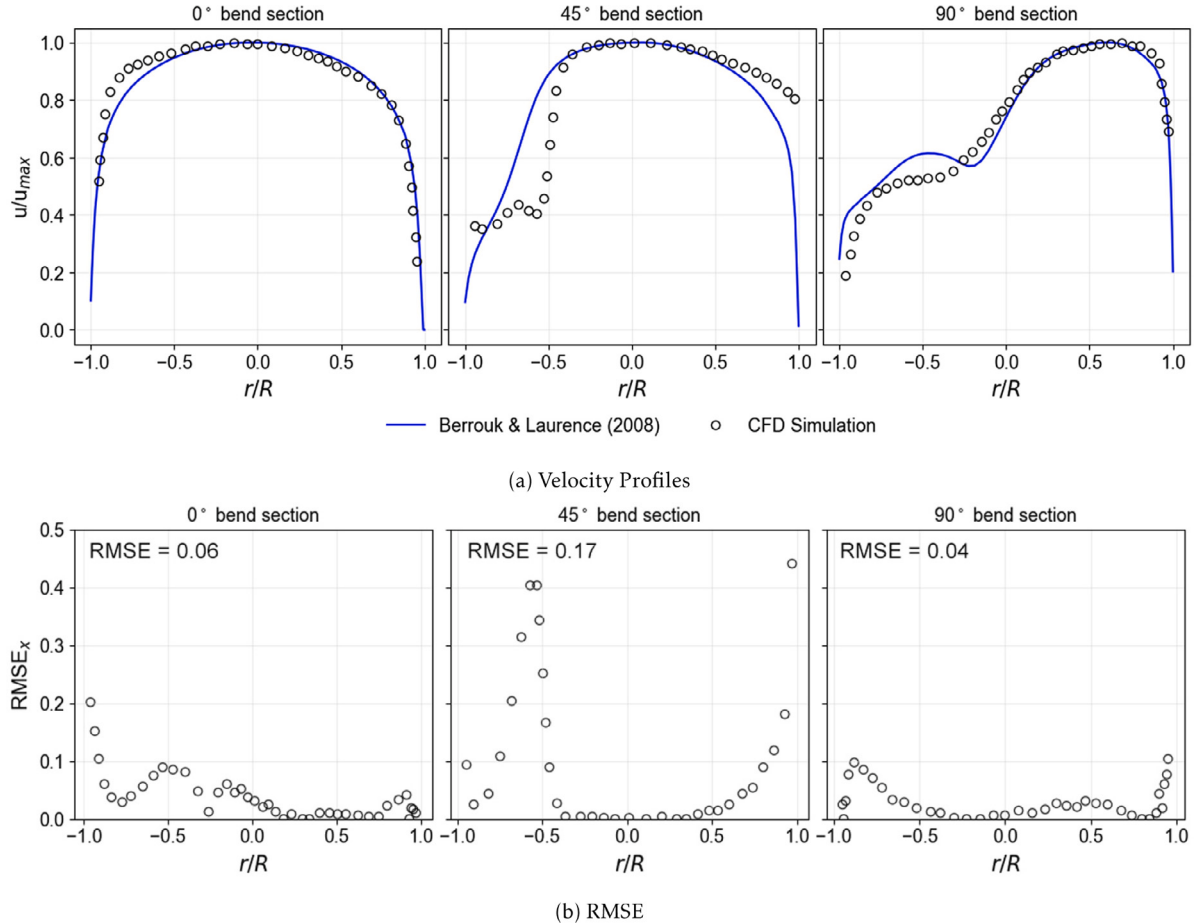


Fig. 4. (a) Comparison of velocity profiles at the bend entry (0°), bend (45°) and bend exit (90°). The black markers were taken from an LES study by [Berrouk and Laurence \(2008\)](#) and the blue line is the current study. (b) An RMSE (Root Mean Square Error) plot is given to quantify the differences between the two results shown in (a). (For interpretation of the references to color in this figure legend, the reader is referred to the web version of this article.)

profiles were plotted for 0° (bend inlet), 45° and 90° (bend exit) locations (Fig. 4). The general trend was captured well by the current CFD simulation using the $k\omega$ -SST model compared with the LES study by [Berrouk and Laurence \(2008\)](#). The local Root Mean Square Error is plotted and defined as:

$$\text{RMSE}_x = \sqrt{(x_i - x_o)^2}$$

and the overall RMSE was determined by

$$\text{RMSE} = \sqrt{\frac{1}{N} \sum_{i=1}^N (x_i - x_o)^2}$$

which produced values of 3.9%, 10.6%, and 2.9% for the 0° , 45° , and 90° sections of the pipe bend, respectively. The larger disparity in results at the 45° section is due to the large variations at the inner and outer wall sections of the pipe. In particular is the behaviour at r/R range of -1.0 to -0.5 where the LES results from [Berrouk and Laurence \(2008\)](#) has a flatter profile, while our $k\omega$ -SST result had a gradual velocity increase. In addition, the results of [Berrouk and Laurence \(2008\)](#) did not show the velocity magnitude going to zero at the walls, which caused most of the differences in comparison data.

Particle deposition

Fig. 5 shows the particle deposition under the different particle tracking schemes. The effects of high-resolution tracking on deposition is shown in panel (a). High-resolution tracking is the default option where the original computational cells are decomposed into sub-tetrahedrons (sub-tets) for the particles to move through the sub-tets via barycentric interpolation ([Ansys, 2023](#)). Without High-Resolution tracking, flow variables in particle equations either use cell-centre values or a truncated Taylor series approximation for interpolation. When High-Resolution tracking is off, the higher order schemes (Trapezoidal and Runge-Kutta) predict deposition for all particle diameters well, while the lower order schemes (Implicit and Analytic) overpredict the

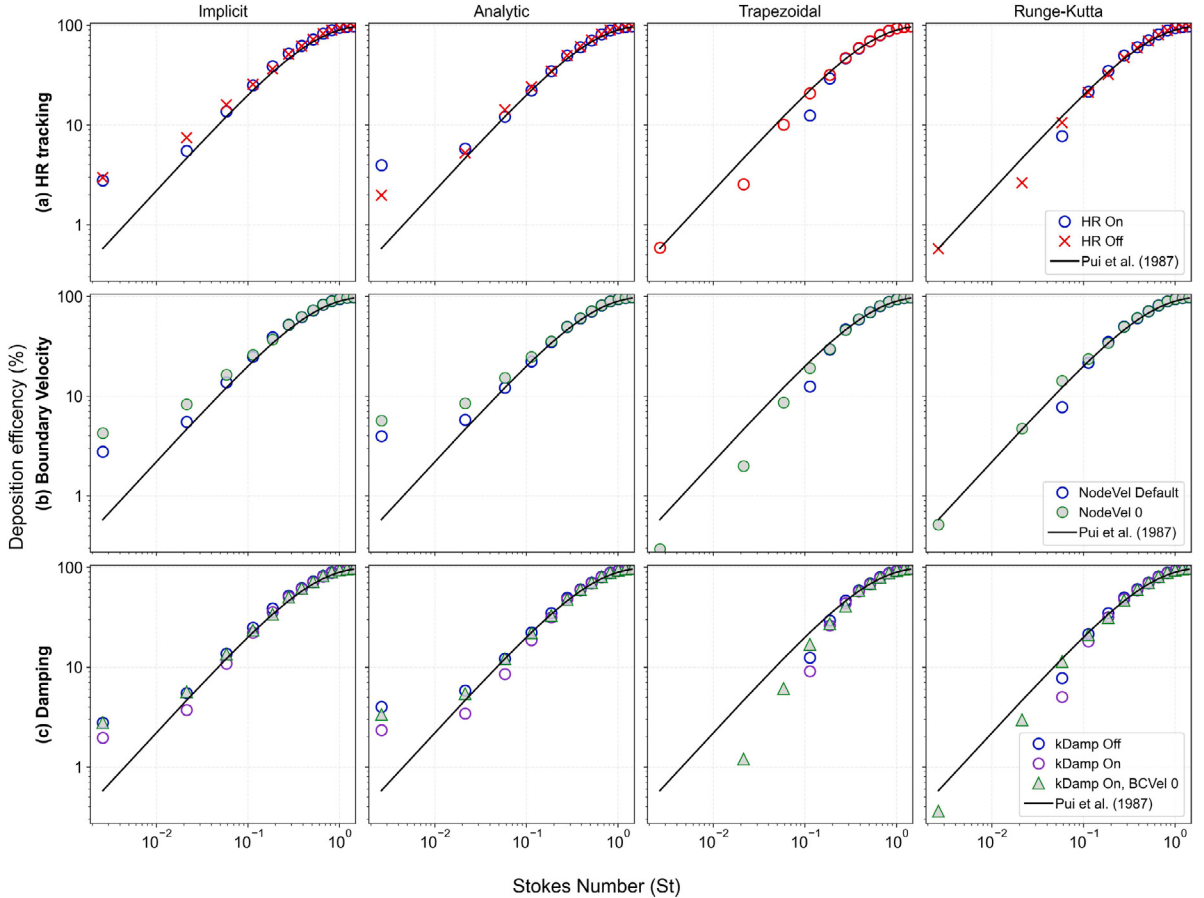


Fig. 5. Assessment of Ansys Fluent Discrete Phase Model settings for particle tracking at $Re = 10,000$. (a) Effect of High Resolution tracking for each numerical scheme. (b) Effect of setting the wall boundary node velocity to zero using the provided TUI command. (c) Effect of implementing the near-wall turbulence correction using a UDF for each numerical scheme with High Resolution tracking.

deposition for low Stokes number particles ($1, 3 \mu\text{m}$). When High-Resolution tracking was enabled (labelled “On”), the Trapezoidal, and Runge-Kutta schemes recorded zero deposition for particles smaller than $5 \mu\text{m}$ and $3 \mu\text{m}$, respectively. However, the lower order schemes recorded deposition for all small particles, although the deposition was higher than the Pui et al. (1987) correlation.

In theory, High-Resolution tracking should improve accuracy through increased integration steps within a cell. However, this was not the case. To overcome the zero deposition found in the higher-order schemes with High-Resolution tracking, we investigated the particle velocity treatment at the wall. By default, nodal velocities on the walls are first reconstructed from cell and face values and then corrected to ensure that there are no velocity components directed towards the walls. This is useful when considering particle impingement on the walls, as the velocity correction will reduce the number of particles that get stuck on walls. However, the velocity correction at the wall nodes may be driving some of the smaller particles away from the walls, and can be disabled by setting a zero nodal velocity on the walls, through the Text-User-Interface (TUI) command:

```
define/models/dpm/numerics/high-resolution-tracking/barycentric-interpolation/zero-nodal-
velocity-on-walls? yes
```

In Fig. 5b High-Resolution tracking is maintained and shows that setting the wall nodal velocities to zero increased particle deposition for the lower particle Stokes number and its effect diminished with increasing particle Stokes numbers. Particle deposition was recorded for all particle sizes in the Trapezoidal and Runge–Kutta schemes, and improved the deposition prediction compared with Pui et al. (1987)'s correlation.

To address the correct physical behaviour of the normal to-the-wall velocity fluctuation (v'), Eq. (24) was applied (the UDF script is given in Appendix A). The equation damps the TKE, thereby reduces the normal to-the-wall velocity fluctuation (v'). Fig. 5c shows the corrected v' reduces the deposition for smaller inertial particles influenced by the velocity fluctuations. Furthermore, the wall nodal velocity correction was applied (green triangle markers) to ensure appropriate particle deposition was recorded for the higher-order schemes.

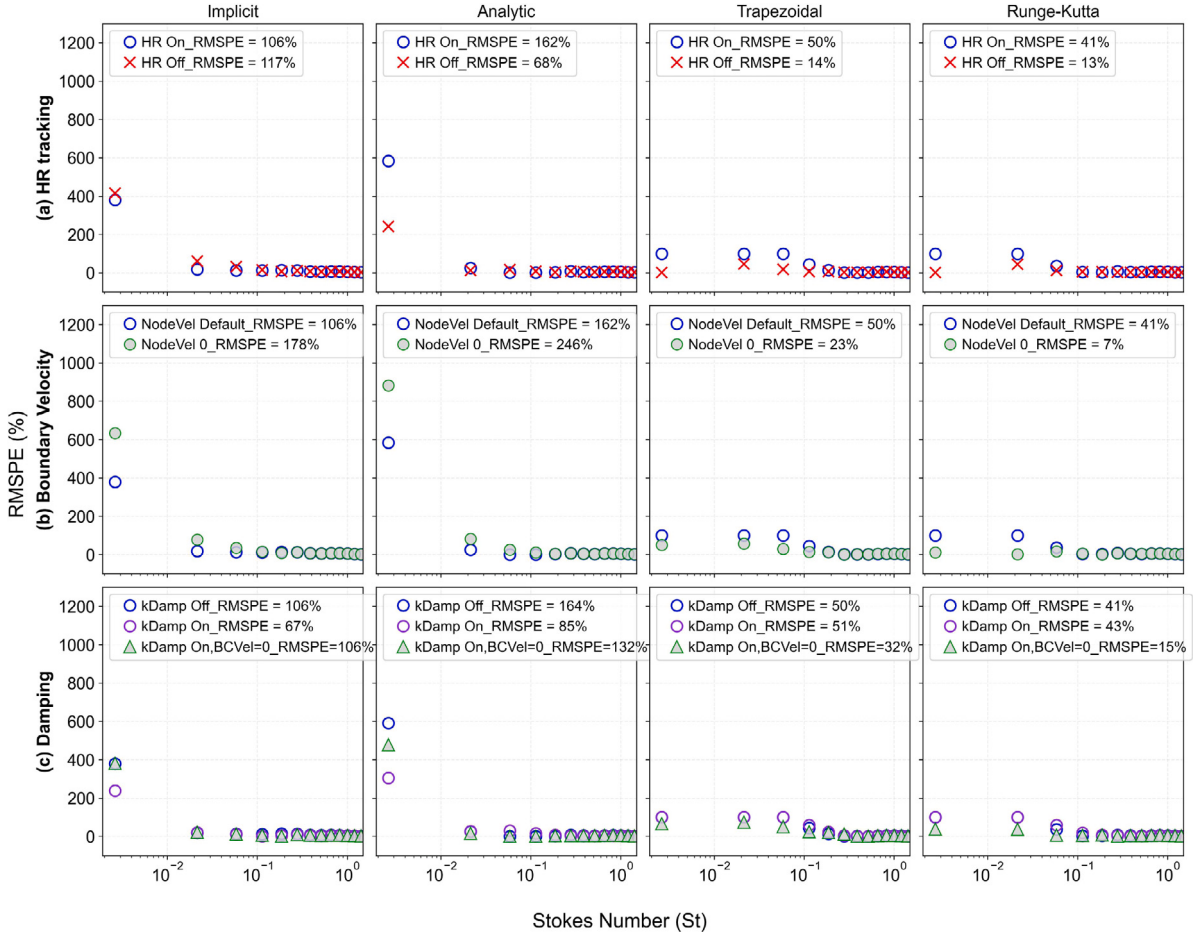


Fig. 6. Root Mean Square Percentage Error analysis for the predicted deposition efficiency variation from the Pui et al. (1987) correlation.

3.2. RMSPE analysis

The predicted results from each particle tracking scheme were quantified using the local Root Mean Square Percentage Error (RMSPE_x) defined as:

$$\text{RMSPE}_x = \sqrt{\left(\frac{x_i - x_o}{x_o} \right)^2}$$

and the overall RMSPE determined by

$$\text{RMSPE} = \sqrt{\frac{1}{N} \sum_{i=1}^N \left(\frac{x_i - x_o}{x_o} \right)^2}$$

Fig. 6 shows the largest variations occur for the low Stokes numbered particles and while these large variations are limited to the 1 to 5 μm particle range, the large local RMSPE_x dominate the overall RMSPE value. Across all settings, the Trapezoidal and Runge-Kutta schemes provide the lowest RMSPE performing significantly better than the Implicit and Analytic schemes. The nodal velocity setting to zero, along with the correct near-wall damping function, provides an acceptable variation of 15% for the Runge-Kutta scheme and 32% for the Analytic scheme. The results highlight the challenges in tracking particles within the 1 to 5 μm diameter range, where they exhibit small particle relaxation times that are sensitive to both flow field changes and particle tracking schemes. The significantly high RMSPE values for the Implicit and Analytic schemes are due to the erroneous predicted deposition values. For example, deposition of 1 μm particles by Pui et al. (1987)'s correlation was 0.577%, and with High Resolution tracking ON (Fig. 6a) the Implicit scheme predicted 2.77% (4.80× greater), while the Analytic scheme produced 3.95% (6.84× greater).

Setting the boundary node velocity to zero with the TKE damping function (Eq. (24)) improved all the results with the High Resolution tracking ON for the higher order Trapezoidal and Runge-Kutta schemes. The boundary node velocity set to zero increased

the deposition for the Implicit and Analytic schemes, thereby deteriorating the predicted results. The Runge–Kutta scheme performed well for the entire particle size range and is an appropriate scheme for particle deposition in this pipe flow.

The default choice in Ansys-Fluent is to use an Automatic particle tracking scheme that switches between a higher and a lower scheme which are the Trapezoidal and Implicit scheme, respectively. The scheme starts with the Trapezoidal scheme but when the solution becomes numerically unstable, the scheme switches to the Implicit scheme that is stable under larger integration steps. Therefore, future studies should verify the predicted solution when dealing with particles that exhibit small Stokes numbers.

Deposition patterns for 1 μm in the pipe bend geometry were plotted for the different settings of High Resolution tracking, boundary node velocity = 0, and damping the turbulence kinetic energy (Fig. 7). The results show locally dominant deposition regions on the inner part of the pipe bend where secondary recirculating flow occurs due to flow separation at the bend. The low inertial 1 μm particle is transported into the inner pipe bend region, leading to deposition. Conversely, higher inertial particles that exhibit inertial impaction as the deposition mechanism will produce deposition patterns closely aligning with the direction of its initial velocity vector, and in the pipe bend, the dominant deposition region is primarily in the outer pipe bend region. Under all settings, the Implicit and Analytic schemes produced significantly greater deposition of 1 μm particles, compared with the Trapezoidal and Runge–Kutta schemes.

3.3. Effect of boundary prism layers

The effects of boundary prism layers are less critical for laminar flows where parabolic profiles exist. However, setting the boundary prism layers is critically important when the flow is turbulent since the flow field in the near wall region needs to be resolved to capture the different turbulent sublayers based on the turbulence model used in the steady Reynolds Averaged Navier–Stokes (RANS) modelling approach. Fig. 8 plots the relative cell-centred node positions relative to the fluid flow represented by the dimensionless velocity, u^+ which matches the $u^+ \approx y^+$. All models had the first cell inside the viscous sublayer, a very thin region near the wall where viscous effects dominate. For the 5-, 8-, and 12-layer models, the number of cells inside the viscous sublayer were 3, 4, and 6, respectively.

Laminar case $Re = 1,000$

A laminar flow field was evaluated first to avoid any dependency of flow turbulence (i.e. near wall turbulence and turbulence particle dispersion) on the particle tracking. A single 5 μm particle was released at a distance of $r/R = 0.8$ from the wall in the straight pipe section, 1D downstream from the inlet, and tracked for up to 500 integration steps. The initial velocity was $v_i/U_{max} = 24$, equating to $v_i = 34.9 \text{ m/s}$, directed towards the wall (v -velocity) to allow the particle to overcome the flow field velocity (u -velocity) and get close to the wall. Fig. 9a shows the x -distance the particle travelled (shown on the x -axis) relative to the distance travelled towards the wall (shown on the y -axis).

The Implicit scheme causes the particle to retain its velocity for longer, leading to deposition on the wall, while the other schemes slow the particle sufficiently, and the particle becomes entrained with the flow field. As the particles approach the wall, they slow down and approach hydrodynamic equilibrium. The higher order Trapezoidal and Runge–Kutta schemes reduce their step length, creating more integration steps, as evidenced by the cluster of steps along the x/R direction, and travelling a shorter distance compared with the Analytic scheme, for the first 500 tracking steps. The trajectories are identical and overlap regardless of the number of boundary prism layers, except for the Analytic scheme. The distances the particle travelled differ for the different number of prism layers, and also among the different integration schemes.

Fig. 9b shows particle tracking for the single 5 μm particle for a turbulent flow, with $Re = 10,000$, while in Fig. 9c the initial velocity was increased to $v_i = 38 \text{ m/s}$ to allow the particle to approach closer to the wall. In all cases, the trajectories are identical, overlapping regardless of the number of boundary prism layers. The differences in trajectories due to the different boundary layer meshing were found for the Trapezoidal scheme, where the 8 layer model extended the particle trajectory for longer. The number of boundary prism layers generally does not influence the particle trajectory (except for the Trapezoidal scheme).

Fig. 10 re-plots the particle's vertical position along the y -axis and its time step size along the x -axis. In all cases, the Trapezoidal and Runge–Kutta time steps were within a similar range of the order of $\Delta t = 1 \times 10^{-4} \text{ s}$. The Implicit scheme exhibited smaller time steps and was typically at least one order of magnitude smaller than the other schemes. The Analytic scheme generally exhibited the largest time steps and this caused the particle to travel the furthest for the first 500 time steps. The particle trajectory was most sensitive to the schemes as the particle moved towards the wall, however when the particle moved away from the near wall region (Fig. 10b), the time steps were similar for the Analytic, Trapezoidal and Runge–Kutta schemes.

The entire motion path for the 5 μm particle in a turbulent $Re = 10,000$ flow under different settings is shown in Fig. 11. The High-Resolution tracking is the default setting in Fluent, and with this setting, the 5 μm particle travels further compared with when the High-Resolution tracking is Off. However, this is adjusted when the wall nodal velocity is set to zero. In all cases, except for the Implicit scheme, the particle trajectories follow the same path. Using the Analytic or Trapezoidal schemes the particles tend to travel further.

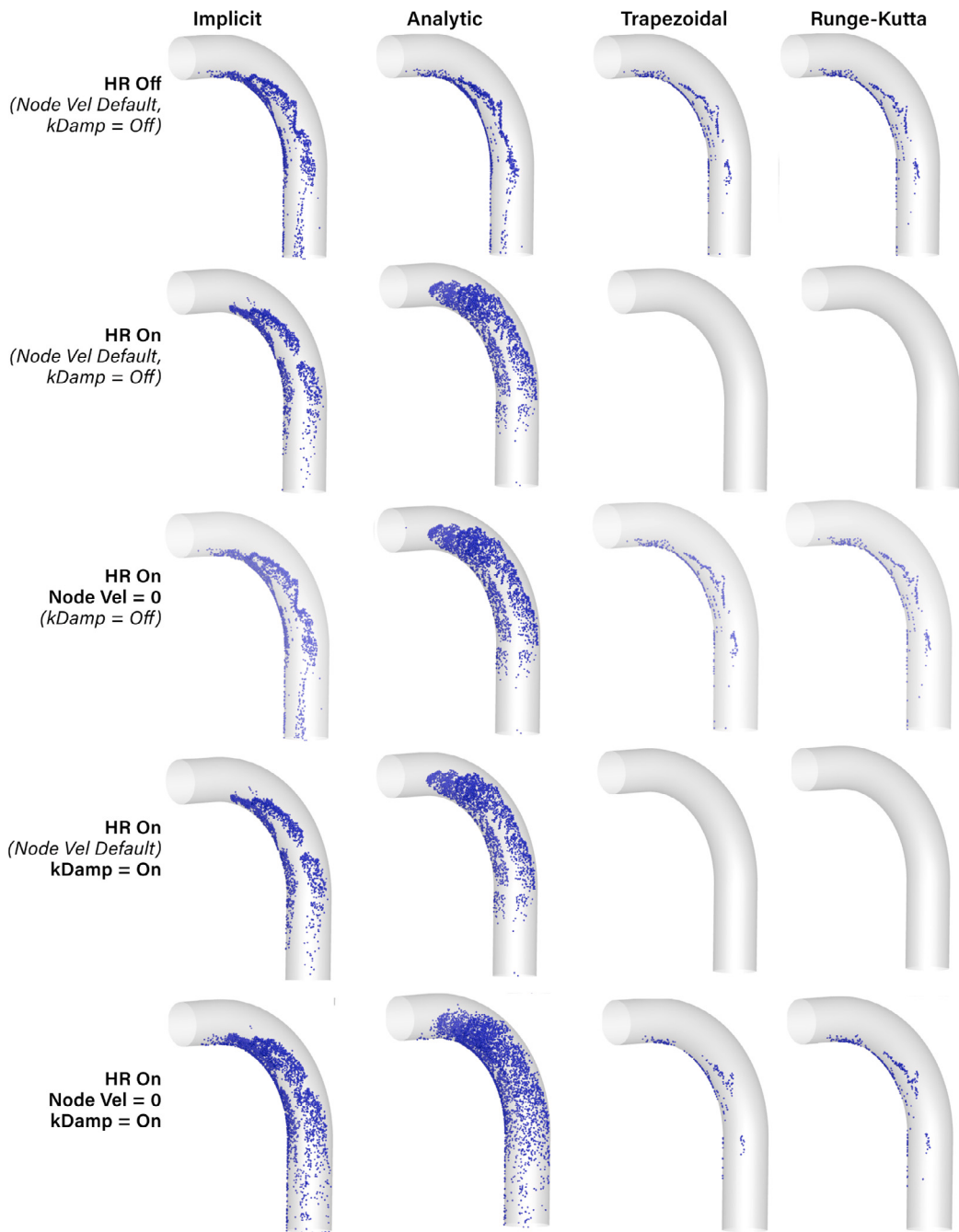


Fig. 7. Particle deposition patterns in 90° pipe bend for 1 μm particles. The contours match the settings provided in Fig. 5.

3.4. Initial particle positions and its deposition

The initial particle positions are coloured by their final particle locations, i.e. deposition on the pipe bend, straight inlet or exit pipe sections, or escaping through the outlet shown in Fig. 12 for all tracking schemes. For 1, 3, and 5 μm particles, that exhibit low inertia (small Stokes number), the dominant region for deposition is found at the top of the pipe inlet surface. As the particle diameter increases, there is a gradual increase in particle positions towards the centre of the pipe. For the 20 μm particles that exhibit high inertia (large Stokes number), nearly the entire surface positions lead to deposition in the bend section. The exception is for the lower part of the inlet surface along the circumference, where these positions lead to deposition in the exit straight pipe section (post bend).

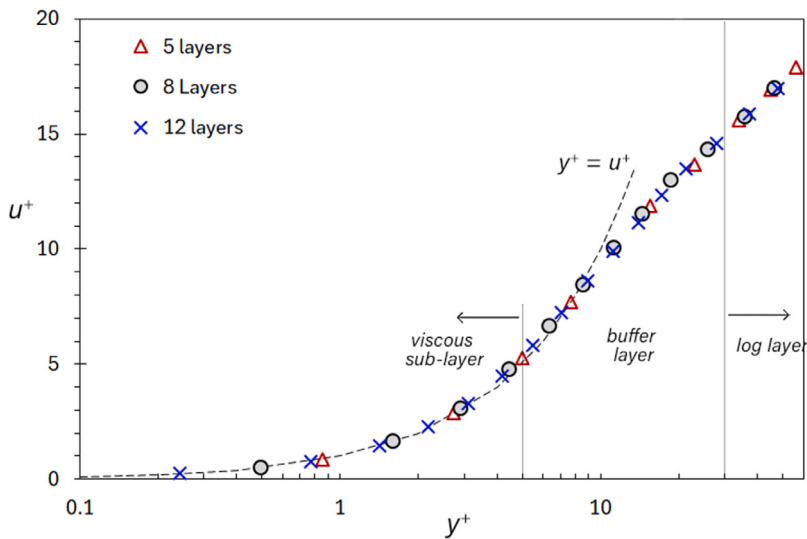


Fig. 8. Mesh nodal positions plotted as a function of u^+ relative to its y^+ . The markers represent all cells away from the wall, and the legend represents each model consisting of the first 5, 8, or 12 markers representing the boundary prism layers.

The locations for deposition are relatively consistent among all tracking schemes, and the differences are found in the amount and coverage within the locations. For example, the Trapezoidal scheme produced the least deposition for 1, 3, and 5 μm particles, and this was shown by the reduced number of positions on the inlet surface, while conversely, the Implicit, and Analytic schemes produced the highest deposition, shown by an increased number of positions on the inlet surface.

Fig. 13 provides visualisation of the trajectories that relates the release position to the final particle position through deposition or escaping from the pipe domain. For the upper inlet release position, the low inertial particles (1, 3, 5 μm) are transported towards the inner wall of the pipe bend from secondary flow phenomena (the Dean vortices), while the 20 μm particles with high inertia impact onto the outer wall of the pipe bend. Particles from the lower inlet release position are less influenced by secondary flow, and escape more readily, except for the 20 μm particles that impact onto the outer wall.

3.5. Nasal cavity deposition

Particle deposition in the nasal cavity was evaluated for the particle tracking schemes for a flow rates of 30 L/min and 60 L/min (Fig. 14) following the 90° pipe bend methodology. As particle deposition in the nasal cavity is primarily governed by inertial impaction, the Inertial Parameter (IP) was used to normalise the deposition behaviour across the different particle diameters (Kelly, Asgharian, Kimbell, & Wong, 2004).

Enabling the High-Resolution tracking reduced the deposition efficiency for all particle sizes under the applied particle integration schemes. A comparison to experimental data from Kelly et al. (2004), indicated that the High-resolution tracking best represents the deposition efficiency for smaller particles. Although zero particle deposition in the pipe for diameters $< 5 \mu\text{m}$ under higher order schemes was observed, these particles were accounted for in the nasal cavity analysis.

Fig. 14b shows the effect of the TUI command for setting the particle wall nodal velocity to zero. The results showed no effect on the deposition for the 1–26 μm particle range under the Implicit, Trapezoidal and Runge–Kutta schemes. However, an increase for all particle sizes was observed for the Analytic scheme. This behaviour was unlike that found for the pipe deposition, where the latter showed a slight increase in deposition for 1, 3, and 5 μm particles.

The near-wall turbulence correction was used to dampen the TKE of the flow field before tracking the particle trajectories (Fig. 14c). Unlike in the deposition in the pipe bend, damping the TKE had a negligible effect on the deposition efficiency for all particle diameters under all numerical schemes. Although Fig. 14b showed that setting the particle wall nodal velocities to zero had no effect on the deposition efficiency when it was combined with the TKE damping, it resulted in a slight increase in deposition efficiency for all numerical schemes.

Fig. 14d repeated the simulation but at a higher flow rate of 60 L/min to demonstrate the influence of increased flow inertia and turbulence generated by the higher flow rate. The influence of the damping function shows a decrease in deposition for particles in the Implicit, Analytic, and Trapezoidal schemes, but did not have an effect for the Runge–Kutta scheme. The addition of the nodal velocity = 0 command, increased deposition for all cases which improved the comparison with Kelly et al. (2004)'s result.

The deposition patterns in the nasal cavity for all schemes are shown in Fig. 15. The 1 and 5 μm particles travelled further through the anatomy and deposited more widely throughout the nasal cavity. The 10 and 20 μm particles produced early deposition in the anterior regions of the nasal cavity in very localised regions where immediate impaction occurred. The Analytic scheme produced a much wider surface coverage than all other schemes and differed significantly from the other schemes. The Implicit scheme provided a deposition pattern similar to the higher order schemes of the Trapezoidal and Runge–Kutta schemes.

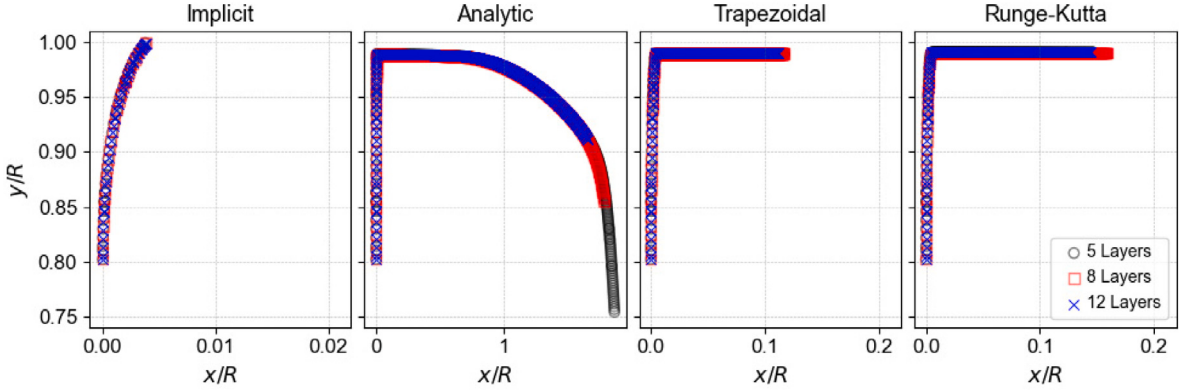
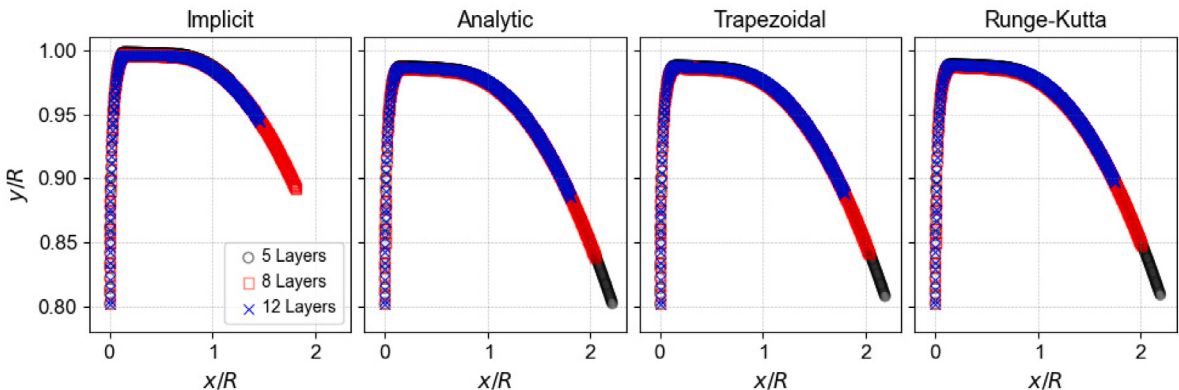
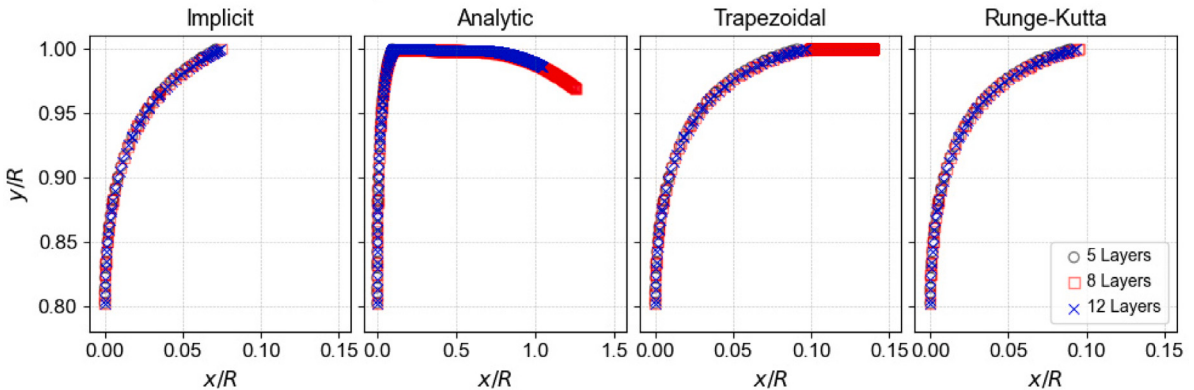
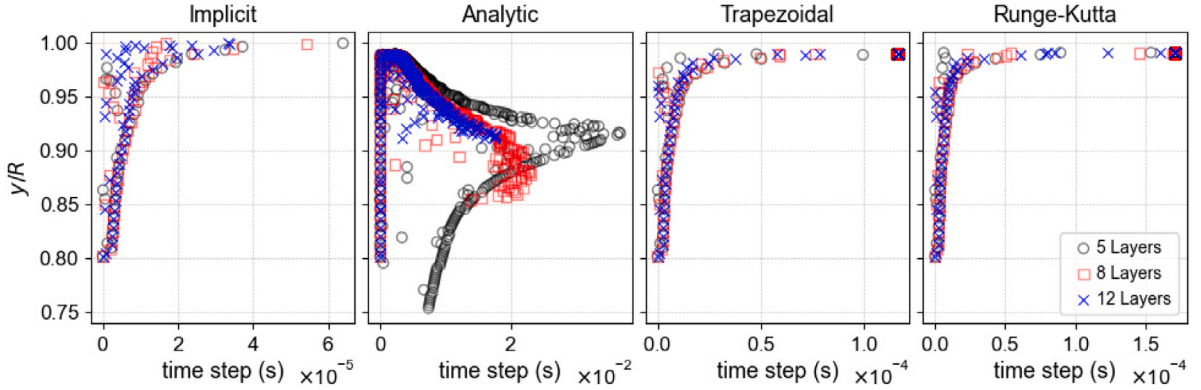
a) Laminar Flow, $Re = 1000$, $v_i = 34.9$ m/sb) Turbulent Flow, $Re = 10\,000$, $v_i = 34.9$ m/sc) Turbulent Flow, $Re = 10\,000$, $v_i = 38$ m/s

Fig. 9. Particle tracking of a $5\ \mu\text{m}$ particle injected towards the wall in the 90° pipe depicting the first 500 integration steps, in (a) laminar flow field with $Re = 1,000$ with an initial velocity of $v_i = 34.9$ m/s, (b) turbulent flow $Re = 10,000$ with an initial velocity of $v_i = 34.9$ m/s, and (c) turbulent flow $Re = 10,000$ with an increase initial particle velocity to $v_i = 38$ m/s. The particle is released from $r/R = 0.8$ of the radial wall distance. The settings used were: High Resolution On; Nodal Vel = 0; and k_damp On for the turbulent case.

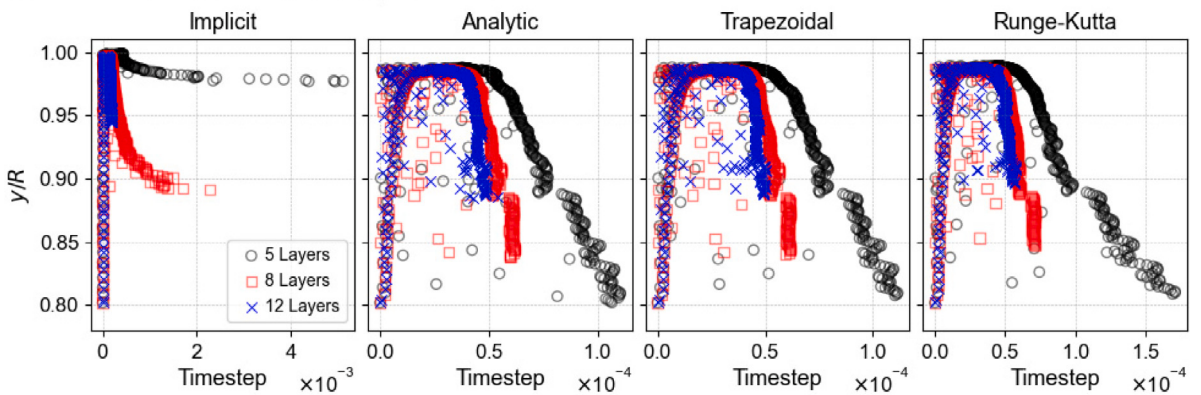
4. Discussion

This study demonstrated the effects of numerical settings in accurately predicting particle deposition in simple and complex geometries. Although the default integration scheme settings used in Ansys-Fluent software provide satisfactory accuracy for simple fluid flow scenarios and particles greater than $5\ \mu\text{m}$ in diameter, there is noticeable variation when dealing with particles less than

a) Laminar Flow, $Re = 1000$, $v_i = 34.9$ m/s



b) Turbulent Flow, $Re = 10\,000$, $v_i = 34.9$ m/s



c) Turbulent Flow, $Re = 10\,000$, $v_i = 38$ m/s

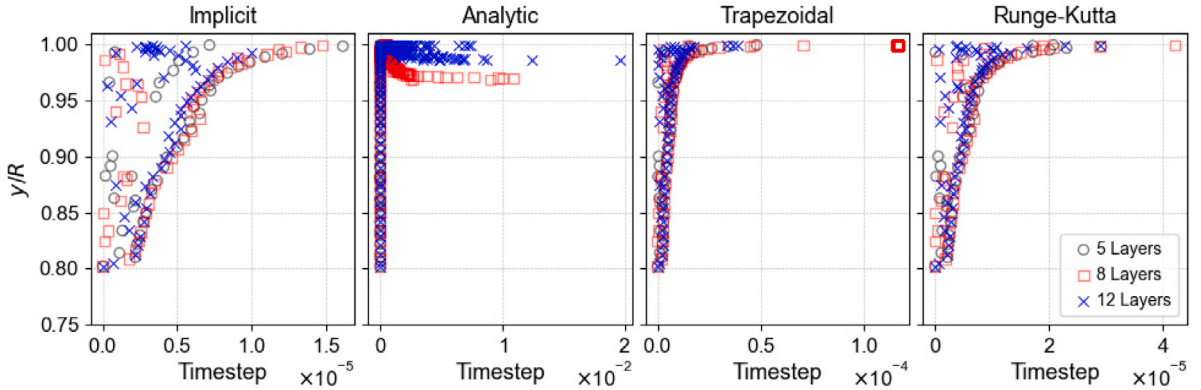


Fig. 10. Particle integration time steps under the integration schemes of a $5\text{ }\mu\text{m}$ injected towards the wall in the 90° pipe depicting the first 500 integration steps, in (a) laminar flow field with $Re = 1,000$ with an initial velocity of $v_i = 34.9$ m/s, (b) turbulent flow $Re = 10,000$ with an initial velocity of $v_i = 34.9$ m/s, and (c) turbulent flow $Re = 10,000$ with an increase initial particle velocity to $v_i = 38$ m/s. The particle is released from $r/R = 0.8$ of the radial wall distance. The settings used were: High Resolution On; Nodal Vel = 0; and k_damp On for the turbulent case.

$5\text{ }\mu\text{m}$. Consequently, it is essential to select the appropriate particle tracking scheme and settings to make sure that reliable results are obtained.

Assessment of the integration scheme confirmed the advantages of Runge–Kutta and Trapezoidal schemes (higher-order schemes) of accuracy but with the cost of additional integration steps when the particle approaches regions of hydrodynamic equilibrium (e.g. in the near wall region). Conversely, the lower-order schemes suffer from truncation errors but provide rapid solutions without limitations on a stable time step range.

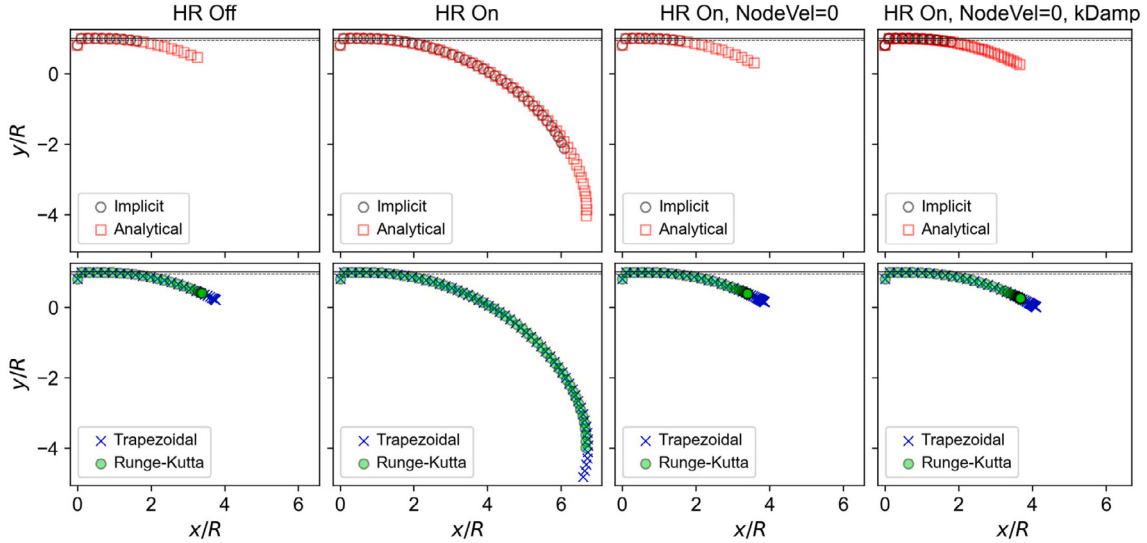
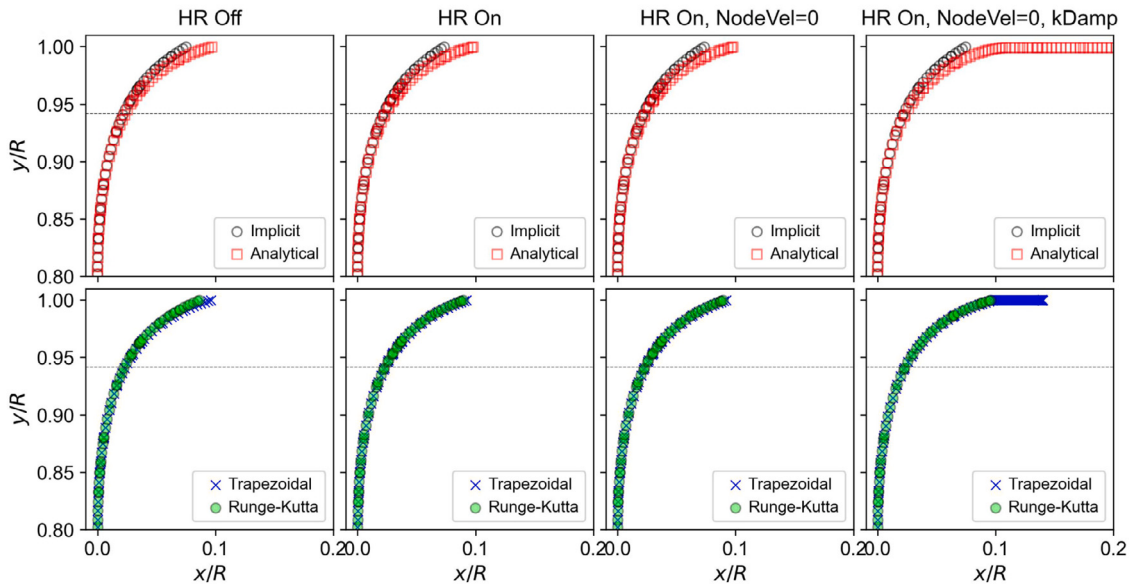
a) $Re = 10\,000, v_i = 34.9 \text{ m/s}$ b) $Re = 10\,000, v_i = 38 \text{ m/s}$ 

Fig. 11. Particle tracking of a $5 \mu\text{m}$ injected towards the wall in the 90° pipe in a turbulent flow $Re = 10,000$ with an (a) initial velocity of $v_i = 34.9 \text{ m/s}$, and (b) initial velocity of $v_i = 38 \text{ m/s}$. The pipe model had 8 prism boundary layers. In each subfigure, the top panel shows the lower-order schemes, and the lower panel shows the higher-order schemes.

The integration time step for each scheme varied and was influenced by the λ (step length factor). In the pipe bend geometry, the Trapezoidal and Runge-Kutta scheme time steps were consistently at least one order of magnitude smaller than those of the Analytic scheme. Varying the λ value may be able to alter the time steps, (subject to mesh sizes as well) and this may improve the tracking capability of the Analytic scheme, but this was out of this study's scope.

In the pipe bend geometry, the Implicit and Analytic schemes tended to overpredict deposition and deviated from the empirical correlation of Pui et al. (1987) with RMSPE in the range of 67–248% for all tests. In comparison, the higher order Trapezoidal and Runge-Kutta schemes provided much better predictions with RMSPE in the range of 7–51%.

The higher order schemes produced zero deposition for particles $< 5 \mu\text{m}$ but this was corrected when setting the wall nodal velocity to zero. The lower order schemes predicted deposition for all particle diameters but there were large overpredictions for particles $< 5 \mu\text{m}$, in the range of RMPSE = 200–600%.

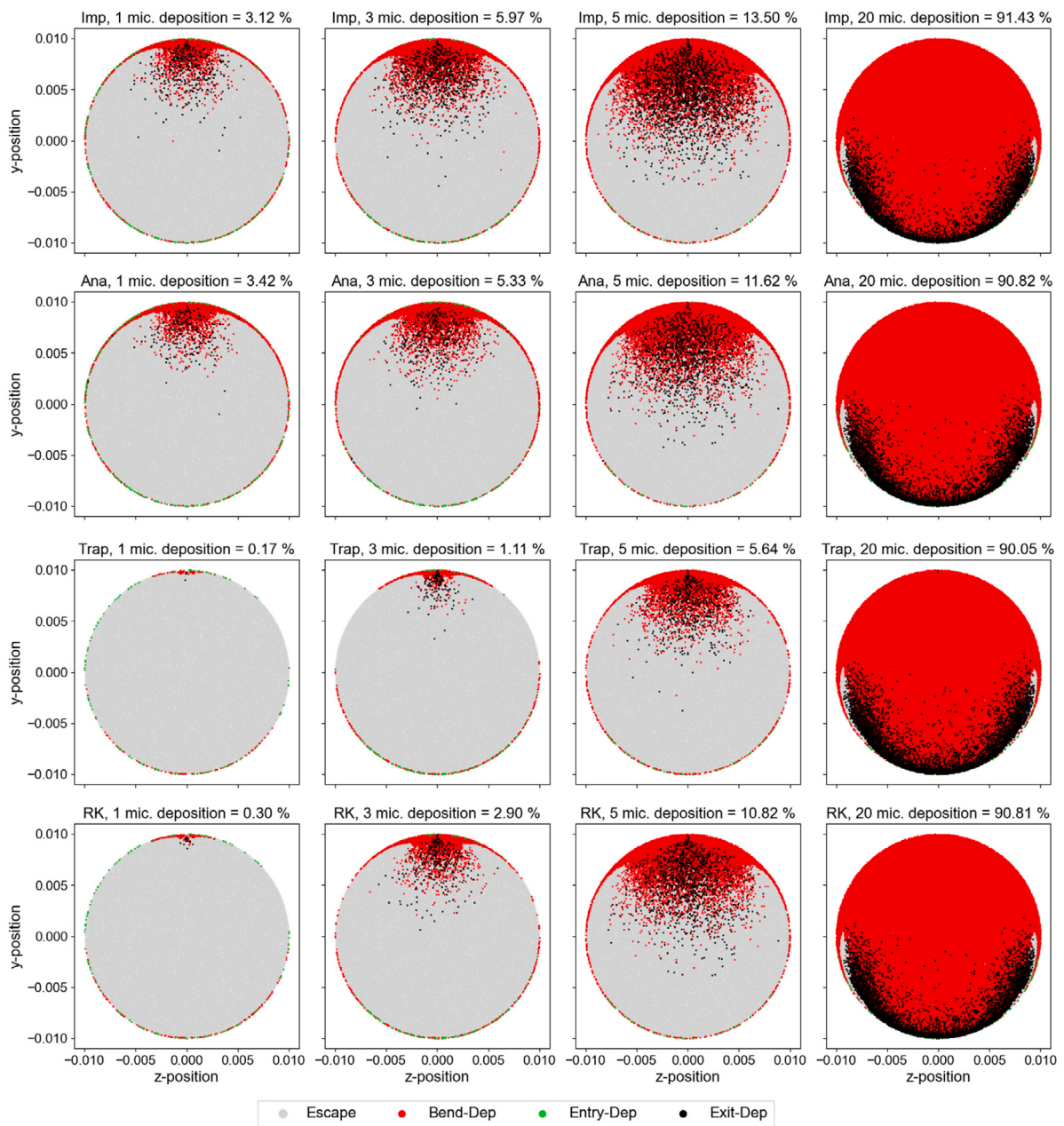


Fig. 12. Initial particle positions at the inlet surface for 1, 3, 5, and 20 μm particles. The positions were coloured by final particle location defined as: escape through the outlet (grey), deposition in the pipe bend section (red), deposition at the straight pipe inlet section (green), or deposition in the straight pipe exit section (black). The settings used were: High Resolution On; Nodal Vel = 0; and k_damp On. (For interpretation of the references to color in this figure legend, the reader is referred to the web version of this article.)

The influence of the number of boundary prism layers was investigated by Bass and Longest (2018) and Frank-Ito et al. (2016). Frank-Ito et al. (2016) concluded that a hybrid mesh containing 4 million tetrahedral cells with three prism layers with a total height of 0.3 mm demonstrated asymptotic behaviour for sinonasal particle deposition, but this was only evaluated for one flow rate. Interestingly, their literature review showed out of 21 cited studies between the years 2005 and 2013, 12 studies did not include any boundary prism layers and the remaining 9 studies applied three to six prism layers. Bass and Longest (2018) demonstrated effects of the number of cell layers, wall y^+ , layer-to-layer ratio, and cell type (hexahedral or tetrahedral), demonstrating four mesh types with a design of "Targeted mesh", with five equally spaced near wall cell layers and a first layer height that gives a wall y^+ of approximately one.

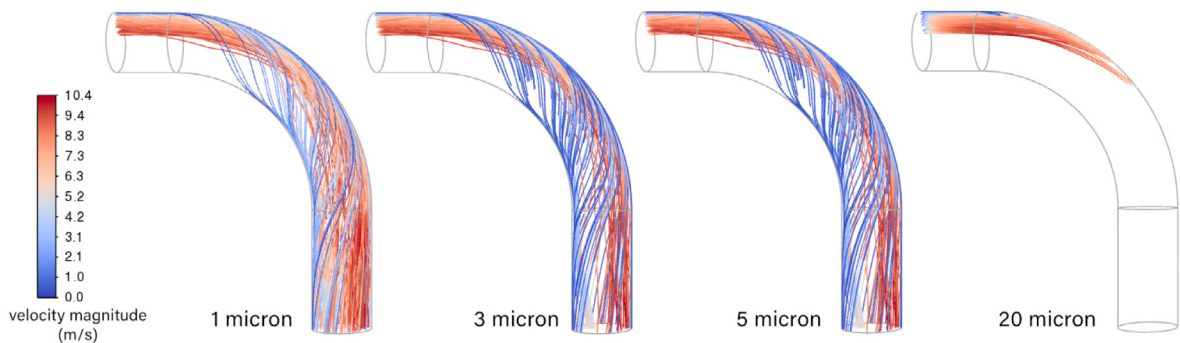
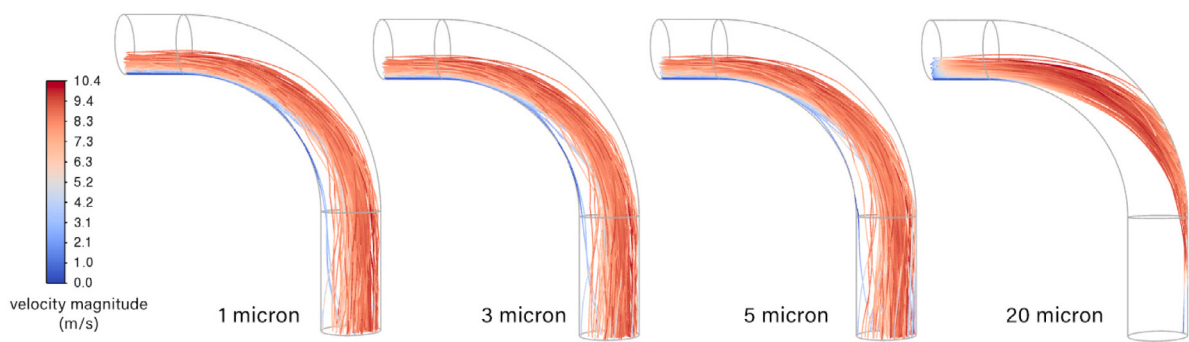
a) Upper inlet release positions**b) Lower inlet release positions**

Fig. 13. Trajectories for 1, 3, 5, and 20 μm particles released from the (a) upper inlet release position, and (b) lower inlet release position. The settings used were: High Resolution On; Nodal Vel = 0; and k_damp On using the Runge-Kutta scheme.

We evaluated the influence of 5, 8, and 12 prism boundary layers, where the near wall flow field was resolved sufficiently. Therefore, increases in the number of prism layers should not influence particle tracking when the flow field solution has converged (does not change with changes in mesh). Since the particle track moves through each cell during its integration steps, increases in a mesh independent model should not affect the particle tracking. Therefore, if the flow field is resolved correctly (Fig. 8), the particle trajectories should be predicted consistently and independently of the mesh density shown in Fig. 9. In this study we applied 8 prism layers with the first mesh node from the wall placed within the viscous sub-layer.

High-resolution tracking is the default option in Fluent; however, in the pipe geometry, it caused the 1 and 3 μm particles to escape when using Trapezoidal and Runge-Kutta schemes. To overcome this, the command to turn on wall nodal velocity to zero was applied which recovered the deposition values. In the nasal cavity results, this effect also helped to increase the deposition when the nodal velocity was set to zero and also helped to improve deposition predictions in the Trapezoidal and Runge-Kutta schemes. When applied to the Analytic scheme deposition was increased for all particles in the pipe and nasal cavity models. Furthermore, localised deposition patterns in the pipe geometry (Fig. 7) show the Analytic scheme exhibits widely dispersed deposition compared with the other schemes. This indicates that the scheme may not be suitable for predicting local deposition patterns despite it being the default choice in Fluent's Automatic numerical scheme.

Applying the TKE damping UDF resulted in global reduction of deposition efficiency in the pipe bend. However, this was not the case for the nasal cavity simulations, with a negligible reduction (less than 1%) observed for all schemes at a flow rate of 30 L/min. When the nasal airway flow rate increased to 60 L/min, a decrease in the deposition was found. As the damping function affects the TKE of the flow field, airway flows that exhibit low levels of turbulence will not be influenced greatly. Strien et al. (2021) investigated turbulent flow in a nasal cavity under 30 L/min and showed that the anterior half of the nasal cavity displayed dominantly laminar but disturbed flow behaviour in the form of velocity fluctuations, and only the posterior half of the nasal cavity displayed turbulent activity, characterised by erratic fluctuating velocities, which was enhanced by the wider cross-sectional areas in the coronal plane. This may explain the weak effect the damping function has on the particle deposition in the nasal cavity.

Matida et al. (2004) showed that the TKE damping was critical to overcome large overpredictions of up to 40 \times the correct deposition for small particles (small particle relaxation times, typically < 5 microns). However, it is noted that Matida et al. (2004)'s study was on the oral airway geometry that exhibits much larger cross-sectional areas and a higher flow rate of 90 L/min, where both factors contribute to greater turbulence. Furthermore, earlier studies with relatively high turbulence, applied near wall

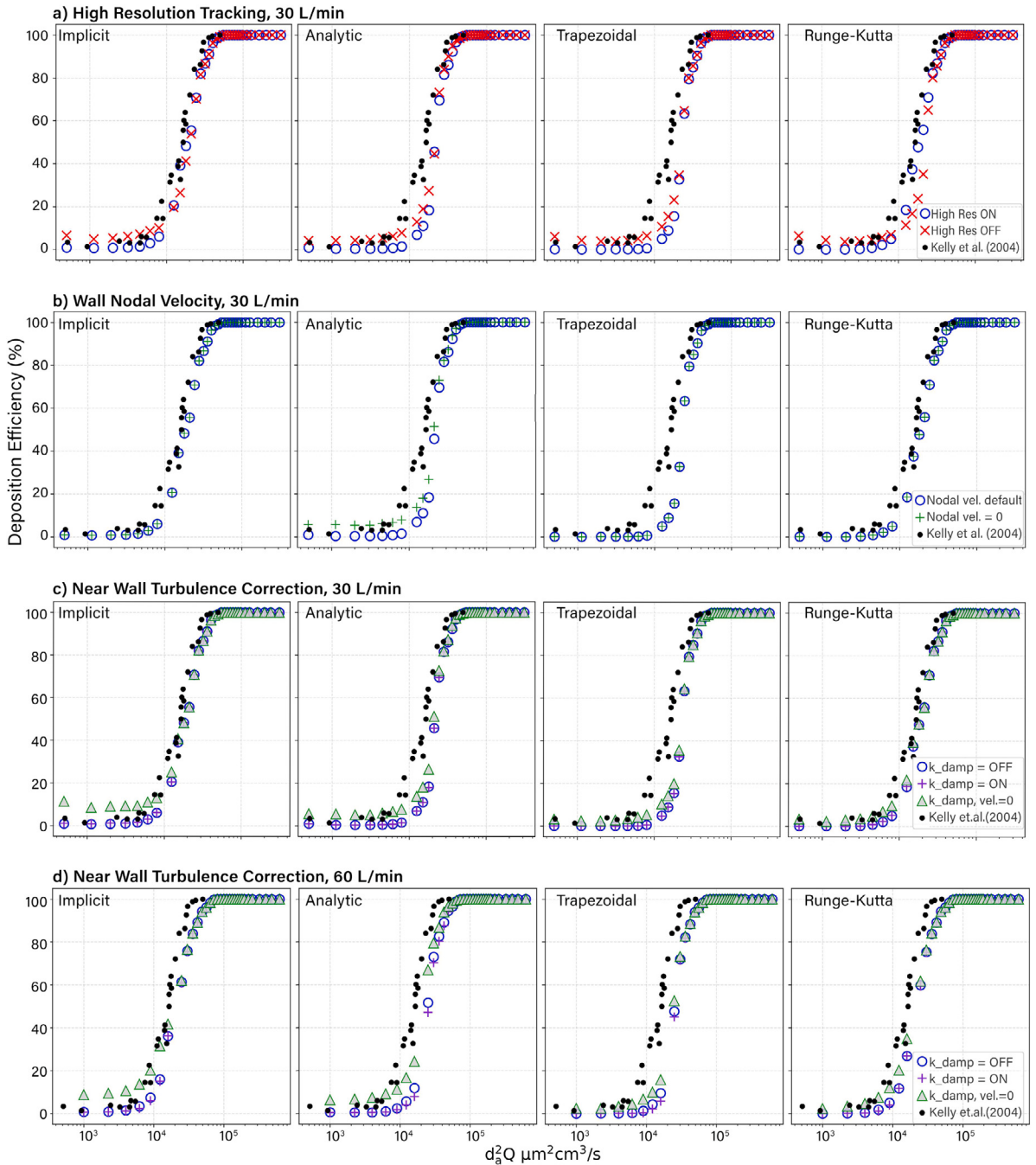


Fig. 14. Assessment of particle deposition efficiency in the human nasal cavity under available discrete phase particle integration schemes, High-resolution tracking and TKE damping for a volumetric flow rate of 30 L/min in (a), (b), and (c), while a flow rate of 60 L/min was used in (d).

corrections that proved useful in validating CFD predictions of aerosol depositions with experimental data (Bass et al., 2021; Bass & Longest, 2018; Longest, Hindle, Choudhuri, & Byron, 2007; Longest & Xi, 2007). Recently, Jubaer et al. (2024) provided new recommendations for simulating aerosol deposition across a range of turbulence levels in tubes and a nasal cavity, which included the application of the low-Re $k-\omega$ model, near wall corrections, and the Eddy-Interaction-Model (the Discrete Random Walk model) modifications. The modifications were tested on two benchmark cases involving turbulent particle deposition in a tube with a 90° bend (Pui et al., 1987) for deposition due to impaction enhanced by turbulent dispersion and a vertical straight pipe (Liu & Agarwal, 1974) dispersion due purely to turbulent dispersion. Therefore, a limitation of this current work was that only the 90° bend deposition was evaluated for deposition due to impaction enhanced by turbulent dispersion.

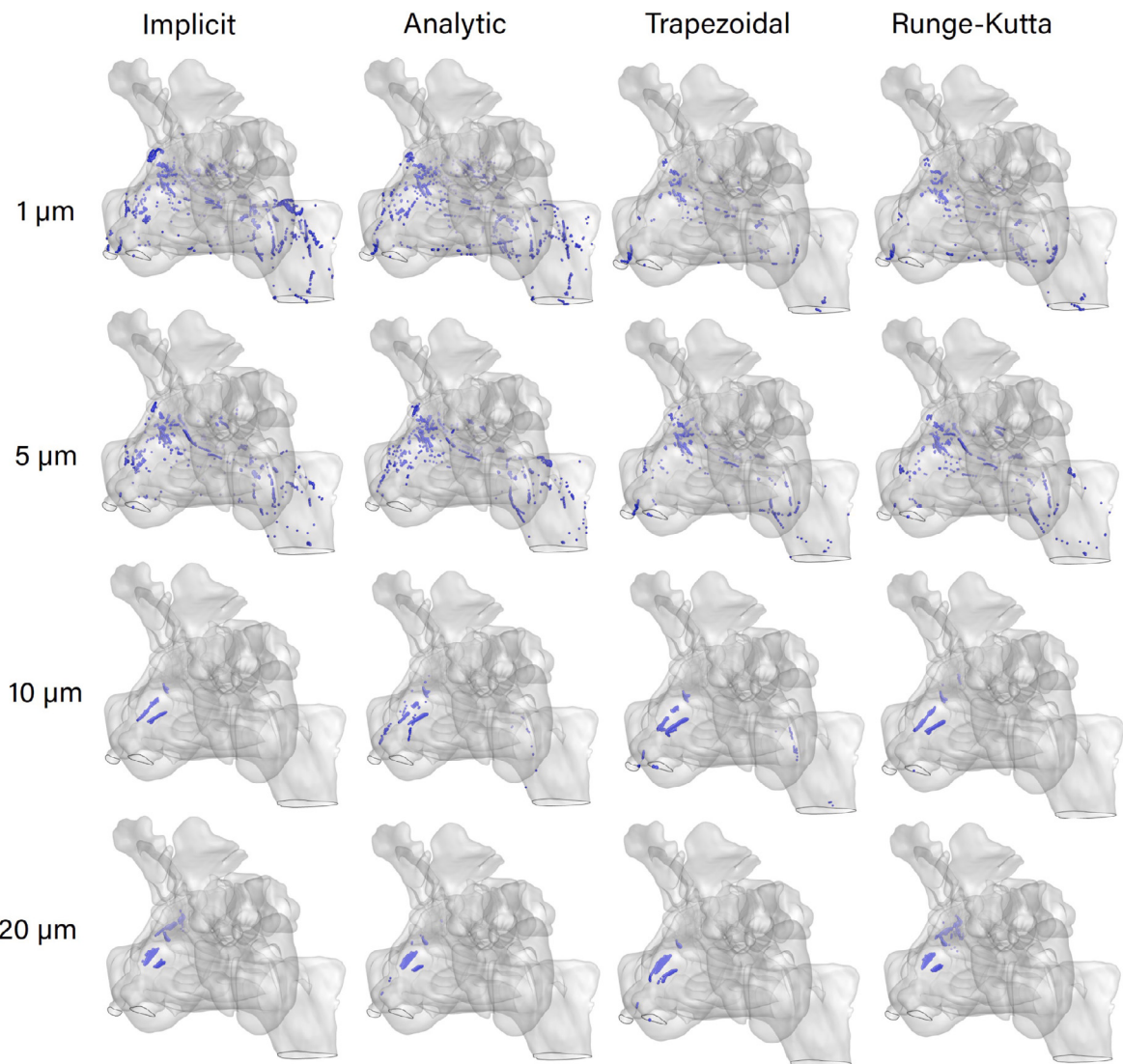


Fig. 15. Particle deposition patterns in nasal geometry at a volumetric flow rate of 30 L/min for particle sizes 1, 5, 10, and 20 μm and each particle integration scheme.

5. Conclusion

Lagrangian particle tracking was performed in Ansys-Fluent (version 2023R2) to evaluate particle tracking schemes of micron-scale particles in a simple pipe bend and complex nasal anatomy model. Significant variation was found in the deposition accuracy between the tracking schemes for particle diameters $< 5 \mu\text{m}$.

The High-Resolution tracking scheme is the default setup for Fluent. When the High-Resolution tracking was applied, an additional TUI command to set the boundary nodal velocities to zero was required to better represent particles $< 5 \mu\text{m}$ for the Trapezoidal and Runge-Kutta schemes in the pipe geometry. However, for the Implicit scheme the High Resolution tracking was the best without the nodal velocity set to zero, while for the Analytic scheme, High Res tracking switched off was the best option. The findings of this study indicate that the Ansys-Fluent Lagrangian tracking of discrete particles is sensitive to multiple parameters and, consequently, should be verified to ensure reliable particle trajectory modelling. In general, we recommend that:

- In turbulent flows, the normal-to-the-wall velocity fluctuation should be damped to better represent the near-wall physics for wall-bounded flows. Its influence is significant in flow fields that exhibit strong turbulence, e.g. pipe bend at $Re = 10,000$, but has weak influence in the nasal cavity at 30 L/min which exhibits low turbulence.
- The High-Resolution tracking scheme is Ansys-Fluent's default setting as it increases integration steps within cells through barycentric interpolating decomposed subset cells. However, it needs verification with the selected numerical schemes. Overall,

using the High-resolution tracking, the Runge–Kutta scheme works best as the general scheme with the TUI command to set the particle wall nodal velocity to zero was applied.

- All particle tracking schemes performed well and are suitable for predicting deposition for particle diameters $> 5 \mu\text{m}$, with high-order resolution tracking and setting the wall nodal velocity to zero.
- The results become sensitive to the particle scheme when dealing with particle diameters $< 5 \mu\text{m}$. The lower-order schemes overpredict deposition, while the higher-order schemes have zero deposition in the pipe bend, unless the wall nodal velocity is set to zero.

In summary, this study has offered suggestions for Ansys Fluent particle trajectory configurations to produce reliable particle deposition in a pipe bend and a human nasal cavity.

CRediT authorship contribution statement

Patrick Warfield-McAlpine: Writing – original draft, Visualization, Validation, Methodology, Investigation. **David F. Fletcher:** Writing – review & editing, Supervision, Investigation, Formal analysis. **Kiao Inthavong:** Writing – review & editing, Visualization, Validation, Supervision, Project administration, Methodology, Investigation, Funding acquisition, Formal analysis, Data curation, Conceptualization.

Declaration of competing interest

The authors declare that they have no known competing financial interests or personal relationships that could have appeared to influence the work reported in this paper.

Data availability

Data will be made available on request.

Acknowledgements

The authors acknowledge the financial support from RMIT's RTP Stipend Scholarship, Australia (RSS). This project was undertaken with the assistance of RMIT University's allocations of resources and services from the National Computational Infrastructure (NCI), which is supported by the Australian Government. The authors thank Ansys support for their in depth explanations on the Fluent DPM code to help shape this study.

Appendix A. Supplementary data

Supplementary material related to this article can be found online at <https://doi.org/10.1016/j.jaerosci.2024.106351>.

References

- Abouali, O., Keshavarzian, E., Ghalati, P. F., Faramarzi, A., Ahmadi, G., & Bagheri, M. H. (2012). Micro and nanoparticle deposition in human nasal passage pre and post virtual maxillary sinus endoscopic surgery. *Respiratory Physiology & Neurobiology*, 181(3), 335–345.
- Abritis, A., Marcus, A., & Oransky, I. (2021). An “alarming” and “exceptionally high” rate of COVID-19 retractions? *Accountability in Research*, 28(1), 58–59.
- Ahmadi, G., Unnis, H., & McLaughlin, J. B. (1992). Numerical simulation of Brownian particle diffusion in a turbulent channel flow. In *Studies in applied mechanics*: vol. 31, (pp. 433–442). Elsevier.
- Ansys, F. (2023). Fluent user's manual. *Software release, 13*.
- Ball, M., & Mitchell, J. (1992). The deposition of micron-sized particles in bends of large diameter pipes. *Journal of Aerosol Science*, 23, 23–26.
- Bass, K., Farkas, D., Hassan, A., Bonasera, S., Hindle, M., & Longest, P. W. (2021). High-efficiency dry powder aerosol delivery to children: Review and application of new technologies. *Journal of Aerosol Science*, 153, Article 105692.
- Bass, K., & Longest, P. W. (2018). Recommendations for simulating microparticle deposition at conditions similar to the upper airways with two-equation turbulence models. *Journal of Aerosol Science*, 119, 31–50.
- Berrouk, A. S., & Laurence, D. (2008). Stochastic modelling of aerosol deposition for LES of 90° bend turbulent flow. *International Journal of Heat and Fluid Flow*, 29(4), 1010–1028.
- Bradshaw, K., Warfield-McAlpine, P., Vahaji, S., Emmerling, J., Salati, H., Sacks, R., et al. (2022). New insights into the breathing physiology from transient respiratory nasal simulation. *Physics of Fluids*, 34(11).
- Breuer, M., Baytekin, H. T., & Matida, E. A. (2006). Prediction of aerosol deposition in 90° bends using LES and an efficient Lagrangian tracking method. *Journal of Aerosol Science*, 37(11), 1407–1428.
- Calmet, H., Kleinstreuer, C., Houzeaux, G., Kolanjiyil, A. V., Lehmkuhl, O., Olivares, E., et al. (2018). Subject-variability effects on micron particle deposition in human nasal cavities. *Journal of Aerosol Science*, 115, 12–28.
- Cash, J. R., & Karp, A. H. (1990). A variable order Runge-Kutta method for initial value problems with rapidly varying right-hand sides. *ACM Transactions on Mathematical Software*, 16(3), 201–222.
- Corley, R. A., Kabilan, S., Kuprat, A. P., Carson, J. P., Minard, K. R., Jacob, R. E., et al. (2012). Comparative computational modeling of airflows and vapor dosimetry in the respiratory tracts of rat, monkey, and human. *Toxicological Sciences*, 128(2), 500–516.
- Dastan, A., Abouali, O., & Ahmadi, G. (2014). CFD simulation of total and regional fiber deposition in human nasal cavities. *Journal of Aerosol Science*, 69, 132–149.
- Dehbi, A. (2008a). A CFD model for particle dispersion in turbulent boundary layer flows. *Nuclear Engineering and Design*, 238(3), 707–715.

- Dehbi, A. (2008b). Turbulent particle dispersion in arbitrary wall-bounded geometries: A coupled CFD-Langevin-equation based approach. *International Journal of Multiphase Flow*, 34(9), 819–828.
- Dinis-Oliveira, R. J. (2020). COVID-19 research: Pandemic versus “paperdemic”, integrity, values and risks of the “speed science”. *Forensic Sciences Research*, 5(2), 174–187.
- Dong, J., Shang, Y., Tian, L., Inthavong, K., Qiu, D., & Tu, J. (2019). Ultrafine particle deposition in a realistic human airway at multiple inhalation scenarios. *International Journal for Numerical Methods in Biomedical Engineering*, 35(7), Article e3215.
- Else, H. (2020). COVID IN PAPERS. *Nature*, 588(24/31), 553.
- Frank-Ito, D. O., Wofford, M., Schroeter, J. D., & Kimbell, J. S. (2016). Influence of mesh density on airflow and particle deposition in sinonasal airway modeling. *Journal of Aerosol Medicine and Pulmonary Drug Delivery*, 29(1), 46–56.
- Garcia, G. J., Schroeter, J. D., & Kimbell, J. S. (2015). Olfactory deposition of inhaled nanoparticles in humans. *Inhalation Toxicology*, 27(8), 394–403.
- Ghalati, P. F., Keshavarzian, E., Abouali, O., Faramarzi, A., Tu, J., & Shakibafard, A. (2012). Numerical analysis of micro-and nano-particle deposition in a realistic human upper airway. *Computers in Biology and Medicine*, 42(1), 39–49.
- Gonda, I., & Gipps, E. (1990). Model of disposition of drugs administered into the human nasal cavity. *Pharmaceutical Research*, 7, 69–75.
- Hofmann, W. (2011). Modelling inhaled particle deposition in the human lung—A review. *Journal of Aerosol Science*, 42(10), 693–724.
- Inthavong, K., Chetty, A., Shang, Y., & Tu, J. (2018). Examining mesh independence for flow dynamics in the human nasal cavity. *Computers in Biology and Medicine*, 102, 40–50.
- Inthavong, K., Ge, Q., Se, C. M., Yang, W., & Tu, J. (2011). Simulation of sprayed particle deposition in a human nasal cavity including a nasal spray device. *Journal of Aerosol Science*, 42(2), 100–113.
- Inthavong, K., Shang, Y., Del Gaudio, J. M., Wise, S. K., Edwards, T. S., Bradshaw, K., et al. (2021). Inhalation and deposition of spherical and pollen particles after middle turbinate resection in a human nasal cavity. *Respiratory Physiology & Neurobiology*, 294, 103769.
- Inthavong, K., Shang, Y., Wong, E., & Singh, N. (2020). Characterization of nasal irrigation flow from a squeeze bottle using computational fluid dynamics. *International Forum of Allergy & Rhinology*, 10(1), 29–40.
- Inthavong, K., Tian, L., & Tu, J. (2016). Lagrangian particle modelling of spherical nanoparticle dispersion and deposition in confined flows. *Journal of Aerosol Science*, 96, 56–68.
- Inthavong, K., Tu, J., & Heschl, C. (2011). Micron particle deposition in the nasal cavity using the v2-F model. *Computers & Fluids*, 51(1), 184–188.
- Ioannidis, J. P., Salholz-Hillel, M., Boyack, K. W., & Baas, J. (2021). The rapid, massive growth of COVID-19 authors in the scientific literature. *Royal Society Open Science*, 8(9), Article 210389.
- Jafari, S., Salmanzadeh, M., Rahnama, M., & Ahmadi, G. (2010). Investigation of particle dispersion and deposition in a channel with a square cylinder obstruction using the lattice Boltzmann method. *Journal of Aerosol Science*, 41(2), 198–206.
- Jubaer, H., Thomas, M., Farkas, D., Kolanjiyil, A. V., Momin, M. A., Hindle, M., et al. (2024). Development of an effective two-equation turbulence modeling approach for simulating aerosol deposition across a range of turbulence levels. *Journal of Aerosol Science*, 175, Article 106262.
- Kelly, J. T., Asgharian, B., Kimbell, J. S., & Wong, B. A. (2004). Particle deposition in human nasal airway replicas manufactured by different methods. Part I: Inertial regime particles. *Aerosol Science and Technology*, 38(11), 1063–1071.
- Kim, J., Moin, P., & Moser, R. (1987). Turbulence statistics in fully developed channel flow at low Reynolds number. *Journal of Fluid Mechanics*, 177, 133–166.
- Kimbell, J. S., Segal, R. A., Asgharian, B., Wong, B. A., Schroeter, J. D., Southall, J. P., et al. (2007). Characterization of deposition from nasal spray devices using a computational fluid dynamics model of the human nasal passages. *Journal of Aerosol Medicine*, 20(1), 59–74.
- Koullapis, P., Kassinios, S. C., Bivolarova, M. P., & Melikov, A. K. (2016). Particle deposition in a realistic geometry of the human conducting airways: Effects of inlet velocity profile, inhalation flowrate and electrostatic charge. *Journal of Biomechanics*, 49(11), 2201–2212.
- Lambert, A. R., O'shaughnessy, P. T., Tawhai, M. H., Hoffman, E. A., & Lin, C.-L. (2011). Regional deposition of particles in an image-based airway model: Large-eddy simulation and left-right lung ventilation asymmetry. *Aerosol Science and Technology*, 45(1), 11–25.
- Li, X., Inthavong, K., Ge, Q., & Tu, J. (2013). Numerical investigation of particle transport and inhalation using standing thermal manikins. *Building and Environment*, 60, 116–125.
- Liu, B. Y., & Agarwal, J. K. (1974). Experimental observation of aerosol deposition in turbulent flow. *Journal of Aerosol Science*, 5(2), 145–155.
- Liu, Y., Matida, E. A., Gu, J., & Johnson, M. R. (2007). Numerical simulation of aerosol deposition in a 3-D human nasal cavity using RANS, RANS/EIM, and LES. *Journal of Aerosol Science*, 38(7), 683–700.
- Longest, P. W., Hindle, M., Choudhuri, S. D., & Byron, P. R. (2007). Numerical simulations of capillary aerosol generation: CFD model development and comparisons with experimental data. *Aerosol Science and Technology*, 41(10), 952–973.
- Longest, P. W., & Holbrook, L. T. (2012). In silico models of aerosol delivery to the respiratory tract—development and applications. *Advanced Drug Delivery Reviews*, 64(4), 296–311.
- Longest, P. W., & Vinchurkar, S. (2007a). Effects of mesh style and grid convergence on particle deposition in bifurcating airway models with comparisons to experimental data. *Medical Engineering & Physics*, 29(3), 350–366.
- Longest, P. W., & Vinchurkar, S. (2007b). Validating CFD predictions of respiratory aerosol deposition: Effects of upstream transition and turbulence. *Journal of Biomechanics*, 40(2), 305–316.
- Longest, P. W., & Xi, J. (2007). Effectiveness of direct Lagrangian tracking models for simulating nanoparticle deposition in the upper airways. *Aerosol Science and Technology*, 41(4), 380–397.
- Matida, E., Finlay, W. H., Lange, C., & Grgic, B. (2004). Improved numerical simulation of aerosol deposition in an idealized mouth–throat. *Journal of Aerosol Science*, 35(1), 1–19.
- Matida, E. A., Nishino, K., & Torii, K. (2000). Statistical simulation of particle deposition on the wall from turbulent dispersed pipe flow. *International Journal of Heat and Fluid Flow*, 21(4), 389–402.
- Mehel, A., Tanière, A., Oesterlé, B., & Fontaine, J.-R. (2010). The influence of an anisotropic Langevin dispersion model on the prediction of micro-and nanoparticle deposition in wall-bounded turbulent flows. *Journal of Aerosol Science*, 41(8), 729–744.
- Menter, F. (1993). Zonal two equation kw turbulence models for aerodynamic flows. In *23rd fluid dynamics, plasmadynamics, and lasers conference* (p. 2906).
- Mofakham, A. A., & Ahmadi, G. (2020). On random walk models for simulation of particle-laden turbulent flows. *International Journal of Multiphase Flow*, 122, Article 103157.
- Moser, R. D., Kim, J., & Mansour, N. N. (1999). Direct numerical simulation of turbulent channel flow up to $Re = 590$. *Physics of Fluids*, 11(4), 943–945.
- Nowak, N., Kakade, P. P., & Annapragada, A. V. (2003). Computational fluid dynamics simulation of airflow and aerosol deposition in human lungs. *Annals of Biomedical Engineering*, 31, 374–390.
- Pui, D. Y., Romay-Novas, F., & Liu, B. Y. (1987). Experimental study of particle deposition in bends of circular cross section. *Aerosol Science and Technology*, 7(3), 301–315.
- Schroeter, J. D., Garcia, G. J., & Kimbell, J. S. (2011). Effects of surface smoothness on inertial particle deposition in human nasal models. *Journal of Aerosol Science*, 42(1), 52–63.
- Schroeter, J. D., Kimbell, J. S., & Asgharian, B. (2006). Analysis of particle deposition in the turbinate and olfactory regions using a human nasal computational fluid dynamics model. *Journal of Aerosol Medicine*, 19(3), 301–313.
- Senanayake, P., Salati, H., Wong, E., Bradshaw, K., Shang, Y., Singh, N., et al. (2021). The impact of nasal adhesions on airflow and mucosal cooling—A computational fluid dynamics analysis. *Respiratory Physiology & Neurobiology*, 293, Article 103719.

- Senanayake, P., Warfield-McAlpine, P., Salati, H., Bradshaw, K., Wong, E., Inthavong, K., et al. (2023). The impact of adhesions on nasal airflow: A quantitative analysis using computational fluid dynamics. *American Journal of Rhinology & Allergy*, 37(3), 273–283.
- Shang, Y., & Inthavong, K. (2019). Numerical assessment of ambient inhaled micron particle deposition in a human nasal cavity. *Experimental and Computational Multiphase Flow*, 1, 109–115.
- Shang, Y., Inthavong, K., & Tu, J. (2015). Detailed micro-particle deposition patterns in the human nasal cavity influenced by the breathing zone. *Computers & Fluids*, 114, 141–150.
- Shi, H., Kleinstreuer, C., & Zhang, Z. (2008). Dilute suspension flow with nanoparticle deposition in a representative nasal airway model. *Physics of Fluids*, 20(1).
- Shrestha, K., Salati, H., Fletcher, D., Singh, N., & Inthavong, K. (2021). Effects of head tilt on squeeze-bottle nasal irrigation—A computational fluid dynamics study. *Journal of Biomechanics*, 123, Article 110490.
- Si, X. A., Xi, J., Kim, J., Zhou, Y., & Zhong, H. (2013). Modeling of release position and ventilation effects on olfactory aerosol drug delivery. *Respiratory Physiology & Neurobiology*, 186(1), 22–32.
- Teixeira da Silva, J. A., Bornemann-Cimenti, H., & Tsigaris, P. (2021). Optimizing peer review to minimize the risk of retracting COVID-19-related literature. *Medicine, Health Care and Philosophy*, 24, 21–26.
- Van Strien, J., Shrestha, K., Gabriel, S., Lappas, P., Fletcher, D. F., Singh, N., et al. (2021). Pressure distribution and flow dynamics in a nasal airway using a scale resolving simulation. *Physics of Fluids*, 33(1), 053312.
- Vinchurkar, S., & Longest, P. W. (2008). Evaluation of hexahedral, prismatic and hybrid mesh styles for simulating respiratory aerosol dynamics. *Computers & Fluids*, 37(3), 317–331.
- Wang, Y., & James, P. (1999). On the effect of anisotropy on the turbulent dispersion and deposition of small particles. *International Journal of Multiphase Flow*, 25(3), 551–558.
- Wang, Q., & Squires, K. (1996). Large eddy simulation of particle deposition in a vertical turbulent channel flow. *International Journal of Multiphase Flow*, 22(4), 667–683.
- Yousefi, M., Inthavong, K., & Tu, J. (2015). Microparticle transport and deposition in the human oral airway: Toward the smart spacer. *Aerosol Science and Technology*, 49(11), 1109–1120.
- Zhang, H., Ahmadi, G., Fan, F.-G., & McLaughlin, J. B. (2001). Ellipsoidal particles transport and deposition in turbulent channel flows. *International Journal of Multiphase Flow*, 27(6), 971–1009.
- Zhang, Z., Kleinstreuer, C., Donohue, J. F., & Kim, C. (2005). Comparison of micro-and nano-size particle depositions in a human upper airway model. *Journal of Aerosol Science*, 36(2), 211–233.
- Zhang, Y., Shang, Y., Inthavong, K., Tong, Z., Sun, B., Zhu, K., et al. (2019). Computational investigation of dust mite allergens in a realistic human nasal cavity. *Inhalation Toxicology*, 31(6), 224–235.